NAVAL POSTGRADUATE SCHOOL

MONTEREY, CALIFORNIA

THESIS

DISTRIBUTED BEAMFORMING IN WIRELESS SENSOR NETWORKS

by

Chan Chee Wai

December 2004

Thesis Advisor:	Murali Tummala
Co-Advisor:	Roberto Cristi

Approved for public release, distribution is unlimited

THIS PAGE INTENTIONALLY LEFT BLANK

REPORT DOCUMENTATION PAGE			*Form Approved OMB No. 0704-0188*
Public reporting burden for this collection of information is estimated to average 1 hour per response, including the time for reviewing instruction, searching existing data sources, gathering and maintaining the data needed, and completing and reviewing the collection of information. Send comments regarding this burden estimate or any other aspect of this collection of information, including suggestions for reducing this burden, to Washington headquarters Services, Directorate for Information Operations and Reports, 1215 Jefferson Davis Highway, Suite 1204, Arlington, VA 22202-4302, and to the Office of Management and Budget, Paperwork Reduction Project (0704-0188) Washington DC 20503.			
1. AGENCY USE ONLY *(Leave blank)*	**2. REPORT DATE** December 2004	**3. REPORT TYPE AND DATES COVERED** Master's Thesis	
4. TITLE AND SUBTITLE: Distributed Beamforming in Wireless Sensor Networks		**5. FUNDING NUMBERS**	
6. AUTHOR(S) Chan Chee Wai			
7. PERFORMING ORGANIZATION NAME(S) AND ADDRESS(ES) Naval Postgraduate School Monterey, CA 93943-5000		**8. PERFORMING ORGANIZATION REPORT NUMBER**	
9. SPONSORING /MONITORING AGENCY NAME(S) AND ADDRESS(ES) N/A		**10. SPONSORING/MONITORING AGENCY REPORT NUMBER**	
11. SUPPLEMENTARY NOTES The views expressed in this thesis are those of the author and do not reflect the official policy or position of the Department of Defense or the U.S. Government.			
12a. DISTRIBUTION / AVAILABILITY STATEMENT Approved for public release, distribution is unlimited		**12b. DISTRIBUTION CODE**	

13. ABSTRACT (maximum 200 words)

A wireless sensor network (WSN) consists of a large number of small sensor nodes that are densely deployed over an area to acquire information about targets of interest. These sensor nodes collaborate among themselves to form an ad-hoc network and disseminate the collected target information to an unmanned aerial vehicle (UAV). The objective is then to increase the data rate and transmission range between the sensor nodes and the UAV. A distributed beamforming approach was proposed whereby the sensor nodes are grouped into clusters and their transmission are coordinated in order to form a distributed antenna array that directs a beam towards the UAV. A simulation model was developed and implemented in MATLAB programming language to study the effectiveness of beamforming using sensor clusters for establishing a communication link to the UAV. Results showed that the antenna main lobe remained relatively unchanged in the presence of position errors and sensor node failures or when the density of the sensor nodes changed. Additionally, the maximum average power gain of the main lobe can be increased by increasing the density of the sensor cluster, thereby increasing the transmission range between the sensor clusters and the UAV.

14. SUBJECT TERMS wireless sensor networks, distributed beamforming, random arrays.			**15. NUMBER OF PAGES** 103
			16. PRICE CODE
17. SECURITY CLASSIFICATION OF REPORT Unclassified	**18. SECURITY CLASSIFICATION OF THIS PAGE** Unclassified	**19. SECURITY CLASSIFICATION OF ABSTRACT** Unclassified	**20. LIMITATION OF ABSTRACT** UL

THIS PAGE INTENTIONALLY LEFT BLANK

DISTRIBUTED BEAMFORMING IN WIRELESS SENSOR NETWORKS

Chan Chee Wai
Civilian, Singapore Ministry of Defense
B.Eng, Nanyang Technological University, Singapore, 1999

Submitted in partial fulfillment of the
requirements for the degree of

MASTER OF SCIENCE IN ENGINEERING SCIENCE
(Electrical Engineering)

from the

NAVAL POSTGRADUATE SCHOOL
December 2004

Author: Chan Chee Wai

Approved by: Murali Tummala
                 Thesis Advisor

                 Roberto Cristi
                 Co-Advisor

                 John P. Powers
                 Chairman, Department of Electrical and Computer Engineering

THIS PAGE INTENTIONALLY LEFT BLANK

ABSTRACT

A wireless sensor network (WSN) consists of a large number of small sensor nodes that are densely deployed over an area to acquire information about targets of interest. These sensor nodes collaborate among themselves to form an ad-hoc network and disseminate the collected target information to an unmanned aerial vehicle (UAV). The objective is then to increase the data rate and transmission range between the sensor nodes and the UAV. A distributed beamforming approach was proposed whereby the sensor nodes are grouped into clusters and their transmission are coordinated in order to form a distributed antenna array that directs a beam towards the UAV.

A simulation model was developed and implemented in MATLAB programming language to study the effectiveness of beamforming using sensor clusters for establishing a communication link to the UAV. Results showed that the antenna main lobe remained relatively unchanged in the presence of position errors and sensor node failures or when the density of the sensor nodes changed. Additionally, the maximum average power gain of the main lobe can be increased by increasing the density of the sensor cluster, thereby increasing the transmission range between the sensor clusters and the UAV.

THIS PAGE INTENTIONALLY LEFT BLANK

TABLE OF CONTENTS

LIST OF FIGURES

x

THIS PAGE INTENTIONALLY LEFT BLANK

LIST OF TABLES

THIS PAGE INTENTIONALLY LEFT BLANK

ACKNOWLEDGMENTS

THIS PAGE INTENTIONALLY LEFT BLANK

EXECUTIVE SUMMARY

A wireless sensor network (WSN) consists of a large number of small sensor nodes that are densely deployed over an area to acquire information about targets of interest. They can be deployed for remote sensing of nuclear, biological, and chemical weapons, potential terrorist attack detection and reconnaissance. These sensor nodes collaborate among themselves to form an ad-hoc network and disseminate the collected target information to an unmanned aerial vehicle (UAV). Advances in sensor and UAV technologies result in higher data volume transfer and longer transmission range between the sensor nodes and the UAV. The objective is then to increase the data rate and transmission range between the sensor nodes and the UAV. A distributed beamforming approach was proposed whereby the sensor nodes are grouped into clusters and their transmission are coordinated in order to form a distributed antenna array that directs a beam towards the UAV.

A simulation model was developed and implemented in the MATLAB programming language to study the application of beamforming using sensor clusters for establishing a communication link to the UAV. Different sensor node densities (i.e., number of sensor nodes per unit area), position errors and sensor node failures were simulated to investigate their effects on the antenna beam generated by the sensor cluster. Results showed that the average sidelobe levels increased while the maximum average power gain decreased when the density of the sensor nodes decreased. However, the shape of the main lobe remained relatively unchanged. Results also showed that the presence of position errors and sensor node failures reduced the maximum average power gain of the antenna beam and increased its sidelobe levels, but the shape of the main lobe remained relatively unchanged. These simulation results were found to be in good agreement with the theoretical results for random arrays.

Since the shape of the antenna main lobe remained relatively unchanged in the presence of position errors and sensor node failures or when the density of the sensor nodes changed, it can be steered towards the UAV in an adaptive manner as the UAV flew over the sensor field independent on the sensor node density, position errors and

sensor node failures. This resulted in a higher signal-to-noise ratio, hence a higher channel capacity. Additionally, the maximum average power gain of the main lobe can be increased by increasing the density of the sensor cluster, thereby increasing the transmission range between the sensor clusters and the UAV.

I. INTRODUCTION

Advances in wireless communications and electronics have enabled the development of low-cost, low-power multifunctional sensor nodes that are small in size [1]. These smart disposable microsensors can be deployed in the battlespace, on the ground, in the air, underwater, in vehicles, inside buildings and on human bodies [2]. A wireless sensor network (WSN) consists of a large number of small sensor nodes that are densely deployed within an area of interest. The initial exact position of the sensor nodes need not be predetermined and they can for example be deployed randomly by an unmanned aerial vehicle (UAV) as shown in Fig. 1.
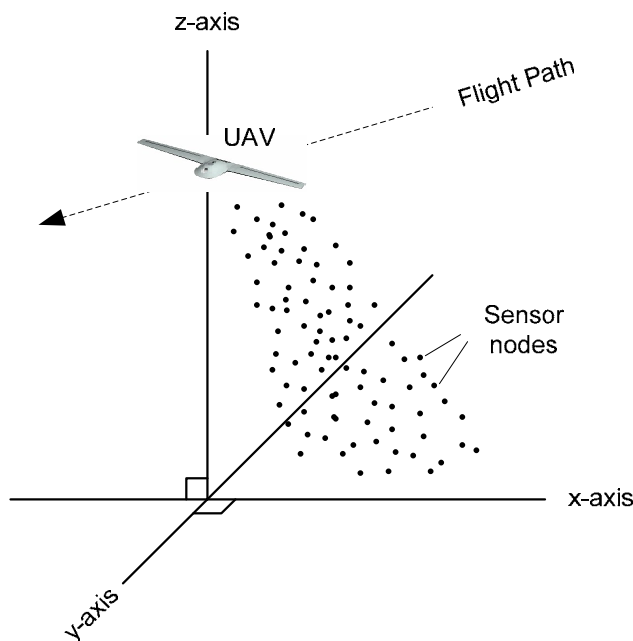
Figure 1.   Random deployment of sensor nodes by an UAV.

These sensor nodes can be deployed quickly and unattended by humans, which make them very attractive for military applications. They can be deployed for remote sensing of nuclear, biological, and chemical weapons, potential terrorist attack detection and reconnaissance [1]. The WSNs provide the option of placing sensor nodes very close to the intended targets of interest without putting human lives at risk.

Once deployed, these multifunctional sensor nodes have the ability to acquire information about targets of interest and collaborate among themselves to form an ad-hoc network and disseminate the collected target information to a relay node. Figure 2 shows how an UAV can receive the data from these sensor nodes in a wireless manner as the UAV flies across the sensor field. The sensor nodes first detect the presence of the UAV, which approaches from an elevation angle of θ_0 and an azimuth angle of ϕ_0 before transmitting the data to the UAV.
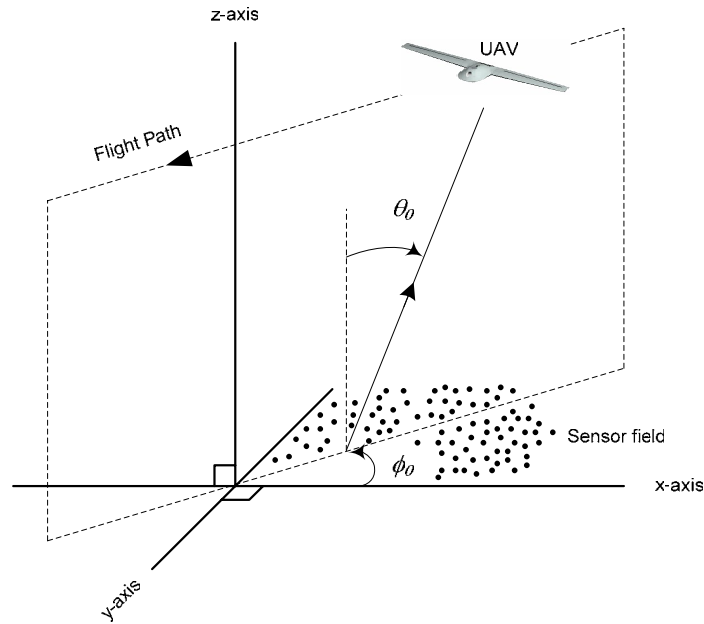
Figure 2.   Wireless data transfer from the sensor nodes to the UAV.

A.   THESIS OBJECTIVE

The operation scenario shown in Figures 1 and 2 is adopted in this thesis. As the sensor technologies improve, more sensor components can be incorporated into the sensor node, which results in more sensing data being collected and higher amounts of data being transmitted to the UAV. Additionally, as the technology improves, the UAVs can fly at higher altitudes and maneuver more efficiently. The objective of this work was to increase the data rate and transmission range between the sensor nodes and the UAV in order to handle the higher data rates and longer transmission ranges required for future military applications.

The ability to handle the increase in data rate and transmission range between each sensor node and the UAV cannot be achieved easily because these sensor nodes are battery-operated and have limited transmission power. In this thesis, a distributed beam-forming approach is proposed whereby the sensor nodes are grouped into clusters and their transmissions are coordinated in order to form a distributed antenna array that directs a beam towards the UAV [6].

The main advantages of using a sensor cluster to form an array-like transmission to the UAV are increased data rate and transmission range. Since the arrays can form a directed beam towards the UAV, the radiated energy is aimed in the direction of the UAV. This increases the signal-to-noise ratio at the UAV and results in increased channel data rate as given by Shannon's formula [3]. Additionally, the fact that a sensor cluster is a type of multiple-input-multiple-output (MIMO) system can be exploited to achieve further data rate gains [4]. The antenna gain obtained from an array of elements can be of several orders higher than that of a single element. This additional antenna gain can extend the transmission range between the sensor nodes and the UAV for a fixed signal-to-noise ratio at the UAV. Other advantages of using arrays include the capability to perform spatial filtering by steering the antenna beam towards the UAV, thereby suppressing interference signals from other directions. Additionally, arrays provide the flexibility to control the antenna gain and beamwidth by changing the number of array elements. These potential benefits make the sensor cluster a suitable candidate to meet the objective stated earlier.

B.   PROBLEM AND PROPOSED SOLUTION APPROACH

The characteristics of sensor clusters are different from those of conventional arrays as given in Table 1. The establishment of conventional arrays is mostly localized. For example, the antenna arrays used for radar and communications are usually localized and installed permanently on site. The beamforming coordination is also performed locally by a central DSP processor, and the positions of the elements and the number of elements are usually predetermined and fixed for a given installation. The array elements also remain operationally active for long periods of time. On the other hand, the establishment of sensor clusters is distributed in nature and the positions of the sensor nodes

are random. The number of sensor nodes required for beamforming is variable. The situation is aggravated by the fact that these sensor nodes can be mobile and subject to frequent failures when their battery energy is depleted or when they are damaged by environmental conditions or human intervention.

No.	Descriptions	Conventional array	Sensor cluster array
1.	Array establishment	Localized	Distributed
2.	Beamforming coordination	Localized	Distributed
3.	Position of elements	Fixed	Random
4.	Number of elements	Fixed	Variable
5.	Position errors of elements	Small	Can be large
6.	Element failures	Few or no element failures	Frequent element failures

Table 1.   Comparison between a conventional array and a sensor cluster.

These differences make the task of distributed beamforming using sensor clusters a challenging problem compared to that of conventional arrays, yet the benefits derived from the higher signal-to-noise ratio (and capacity) gains due to beamforming are significant [6].

The proposed approach for distributed beamforming using sensor cluster is described as follows. Distributed array establishment and beamforming coordination can be achieved by using clustering algorithms to form a hierarchical clustering sensor network architecture. A primary node is elected from among the nodes in each cluster based on some predefined criteria. The primary node is then tasked with maintaining frequency, phase and data synchronization among the remaining nodes (or secondary nodes) within the cluster. The primary node also coordinates the beamforming process to direct an antenna beam towards the UAV in an adaptive manner as the UAV flies across the sensor nodes. The locations of the sensor nodes can be determined using location discovery

methods, such as trilateration and atomic multilateration [16]. While there are existing methods to address the distributed establishment of sensor arrays and determination of sensor node locations, there are no existing methods to address the number of sensor nodes required for beamforming and the presence of position errors and element failures. Therefore, in this thesis, the focus is to tackle these issues by addressing the question on the number of sensor nodes required for beamforming and investigating the effects of position errors and element failures on the quality of the antenna beam generated by the sensor cluster.

In order to address these issues, a simulation model was developed and implemented in the MATLAB programming language, and the results of the simulation are presented.

C.   THESIS OUTLINE

This thesis is organized as follows. Chapter II describes the various WSN architectures and proposes a hierarchical architecture for the selected operational scenario in this thesis. This is followed by the discussion of some existing clustering and location discovery methods for WSN. The ideas of distributed beamforming and using sensor clusters as a MIMO system are also described. Chapter III covers the fundamental principles of antenna arrays, random arrays and adaptive beamforming. The use of arrays to estimate the angle-of-arrival (AOA) and track the desired signal sent from the UAV are also discussed. The significance of the antenna beamwidth on the detection and tracking of the UAV is highlighted. Chapter IV describes the simulation model and presents the simulation results. Chapter V summarizes the work in this thesis and offers several suggestions for future research. Finally, the Appendix contains a description of the MATLAB code used in this work.

THIS PAGE INTENTIONALLY LEFT BLANK

II. INTRODUCTION TO WIRELESS SENSOR NETWORKS

This chapter discusses the various WSN architectures and proposes an architecture for the operational scenario used in this thesis. This is followed by the discussion of some existing clustering and location discovery methods. The advantages of using sensor clusters to increase the transmission range and the channel capacity between the sensor nodes and the UAV are also described in detail.

A.   WIRELESS SENSOR NETWORK (WSN) ARCHITECTURE

Several wireless sensor network (WSN) architectures have been proposed in the literature. Figure 3 shows a general WSN architecture, which consists of a sensor field, a sink node and a satellite through which the user can access the sensor field [1]. A sink node provides the link between the satellite and the sensor nodes, and each sensor node has the ability to route the data to the sink node. For example, the data collected by sensor node *A* is routed back to the sink node through node *B*, *C*, *D* and *E*. The sink node in turn sends the data to the user node via the satellite.
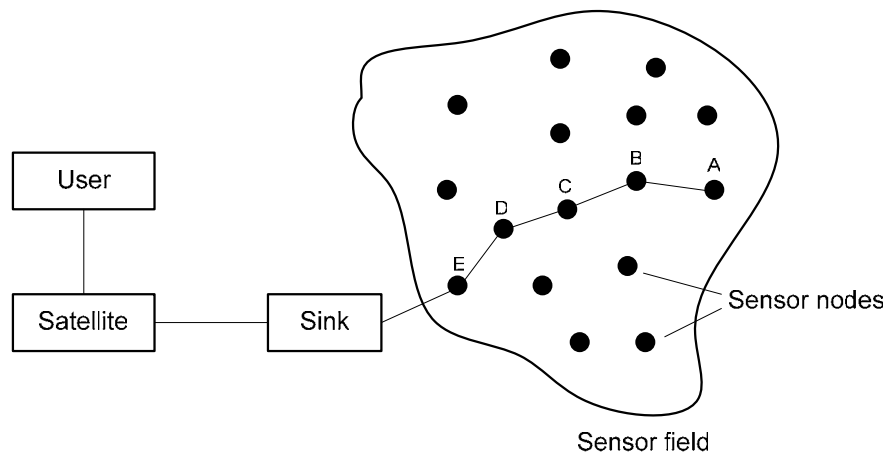
Figure 3.   WSN architecture (After Ref. [1].).

Figure 4 shows a two-tiered hierarchical clustering architecture whereby sensor nodes are autonomously clustered to support energy-efficient and scable operations [9]. A primary node (or cluster head) is elected within each cluster to perform data filtering,

7

fusion and aggregation. The secondary nodes communicate only with the primary node within each cluster while the primary nodes communicate with nodes in the next tier. Sensor clusters are connected with each other through gateway nodes so that data can be transmitted to the higher level nodes if no connectivity exists between a primary node in any cluster in Tier 0 and the nodes in Tier 1. A similar two-tiered architecture has been proposed in [10].
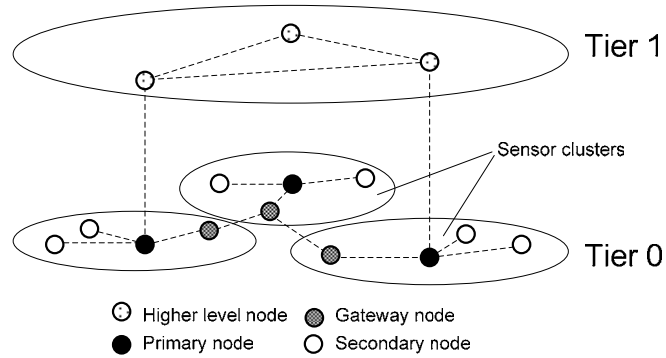
Figure 4.   Two-tiered hierarchical WSN architecture (After Ref. [9].).

Figure 5 shows a three-tiered hierarchical clustering architecture proposed in [11]. It is different from the two-tiered architecture in that there is another tier on top of Tier 1 to consolidate the data. Nodes in Tier 1 communicate with headquarters or a node in Tier 2. The idea of a three-tiered hierarchical clustering architecture was also proposed by [12] and [13].
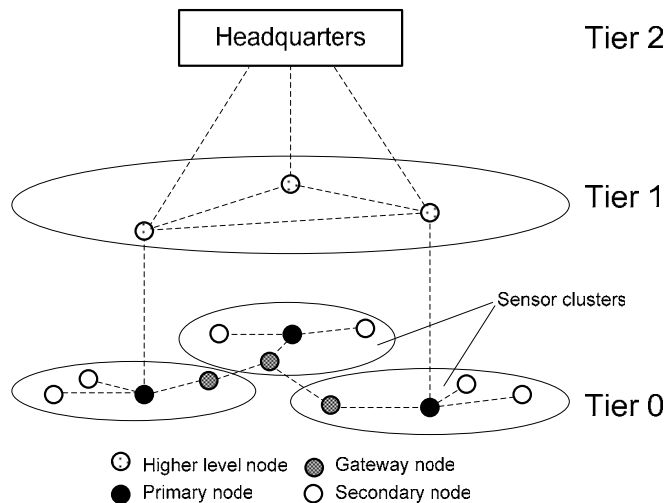
Figure 5.   Three-tiered hierarchical WSN architecture (After Ref. [11].).

The various architectures presented are fairly similar to each other in that they are hierarchical architectures. The main advantages of tiered architecture are scalability, longevity and cost-effectiveness [13]. In this thesis, a three-tiered hierarchical clustering WSN architecture as shown in Fig. 6 is considered. The sensor nodes in Tier 0 are being combined to form clusters, and a primary node is elected within each cluster. The sensor clusters are connected with each other through gateway nodes so that data can be transmitted to the UAV if no connectivity exists between a primary node in any cluster in Tier 0 and the UAVs in Tier 1. The UAVs residing in Tier 1 are organized to communicate to nodes at the next higher tier, which are represented by satellite nodes in this illustration. This aggregation process can be applied repeatedly to form a hierarchy of clusters and allows scalable operation when the number of sensor nodes or UAVs increases due to operational requirements. In this thesis, the focus is on the communication link between the sensor nodes and the UAV.
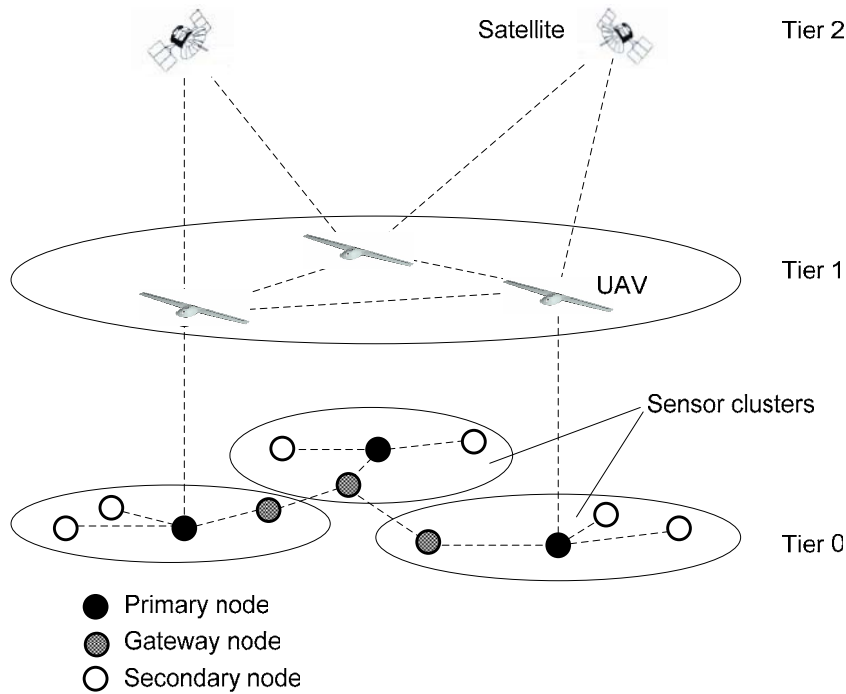
Figure 6.   Proposed three-tiered WSN architecture.

The next section describes some of the clustering methods used to form a hierarchical clustering WSN architecture.

9

B. CLUSTERING IN WSN

The main issues in the hierarchical arrangement shown in Fig. 6 include how to select the primary node and organize the cluster. This section discusses some of the common clustering algorithms that researchers have proposed to address these issues.

1. Lowest ID (LID) Clustering Algorithm

This is a two-hop clustering algorithm, and Fig. 7 shows that a secondary node is at most two hops away from another secondary node within a cluster. According to [14], a sensor node periodically broadcasts the list of nodes (including itself) that it can hear. A sensor node, which only hears nodes with identification (ID) numbers higher than itself from its one-hop neighborhood, declares itself a primary node. The newly declared primary node then sets its own ID number as the cluster ID and broadcasts this information to other nodes. Nodes that are one-hop away from the newly declared primary node receive this information and realize that they are now secondary nodes, leading to the formation of a sensor cluster.

Sensor clusters are linked to adjacent clusters through assigned gateway nodes. For example, in Fig. 7, sensor node 5 is a gateway node that connects clusters 1 and 3. Hence, a sensor node that can hear two or more primary nodes within two hops is a gateway node; otherwise, it is a secondary node. The main disadvantage of this method is that the energy dissipation of the sensor nodes is not evenly distributed within the sensor cluster since the primary node is selected based on ID numbers, and no other attributes, such as node connectivity or energy level, are being accounted for.
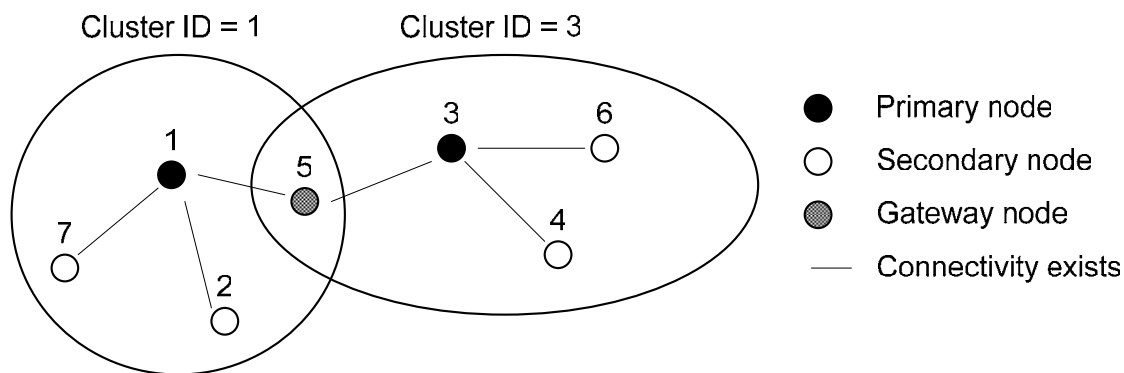
Figure 7.   Lowest ID (LID) clustering algorithm.

2. Highest Connectivity (HCN) Clustering Algorithm

The highest connectivity (HCN) clustering algorithm is similar to the LID algorithm except that a node is elected as the primary node if it has the largest number of connected nodes around it [14]. As shown in Fig. 8, nodes 1 and 3 are elected as primary nodes because both of them have the largest number of connected nodes. This algorithm is better than the LID algorithm in that HCN takes connectivity into account.
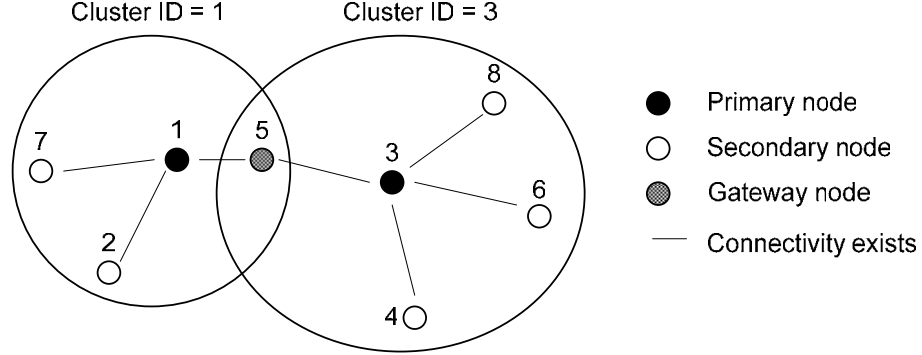
Figure 8.   Highest connectivity (HCN) clustering algorithm.

3. Low-energy Adaptive Clustering Hierarchy (LEACH)

This algorithm aims to minimize the energy dissipation in WSN by changing the primary node assignment periodically so that sensor nodes take turns to perform the role of a primary node for a certain period of time defined as a round. Since data transfer is an energy consuming process and is done by the primary node, this rotation of primary nodes leads to more balanced energy dissipation in the entire network compared to the LID and HCN algorithms.

The LEACH algorithm consists of two phases [15]: setup and steady. During the setup phase, each sensor node chooses a uniform random number between 0 and 1 and if the number is lower than the threshold $T(n)$ for node n, the sensor node becomes the primary node. The threshold $T(n)$ for node n is given by [15]

$$T(n) = \begin{cases} \dfrac{P}{1 - P\left[r\,\mathrm{mod}(1/P)\right]} & \text{if } n \in G \\ 0 & \text{otherwise,} \end{cases} \tag{1}$$

11

where *P* is the desired percentage of sensor nodes that are expected to be primary nodes, *r* is the current round, *G* is the set of sensor nodes that has not been primary nodes in the past 1/*P* rounds and mod( ) denotes the modulus after division. Equation (1) is used to ensure that all sensor nodes dissipate equal amount of energy. Once the primary node has been selected, the next phase is the steady phase in which the primary node assigns a time-division multiple access (TDMA) schedule to the secondary nodes so that the latter can transfer their data to the primary node at predefined time slots. The steady phase lasts for a longer duration than the setup phase. After a certain period of time in the steady phase, the setup phase is initiated again, leading to a change in the primary node assignment.

In summary, three types of clustering algorithms were introduced in this section: primary node selection based on ID numbers, highest connectivity and energy dissipation. Now, we proceed to discuss the task of determining the location of the sensor nodes in the next section.

C. LOCATION DISCOVERY IN WSN

The objective of deploying a WSN is to detect the presence of targets of interest and hence identify their positions. This, in turn, poses a requirement on the sensor nodes to determine their own positions, thus the need for location discovery. This section discusses some of the location discovery techniques that can be used to determine the locations of the sensor nodes, assuming that one or more beacon nodes exist [16]. Beacon nodes are nodes that have absolute information of their own location. Generally, this assumption is valid because in WSN, only a small number of sensor nodes may be equipped with GPS receivers due to economic reasons. They function as location references by periodically broadcasting their location and hence allowing other sensor nodes (not equipped with GPS receivers) to determine their locations.

The common methods of measuring relative distances between beacon nodes and a given node are listed as followed [16]:

　　1.　A given sensor node *A* may use the time of arrival (ToA) techniques to measure the propagation time of a signal emitted by a beacon node *B* and

then calculate the relative distance between itself and the beacon node assuming that the speed of the signal in the medium is known.

2. Time difference of arrival (TDoA) techniques utilize two or more simultaneously transmitted signals from different beacon nodes to determine the time difference between them. The distance from the sensor node to a beacon node can be accurately calculated using the measured TDoA.

3. A sensor node may also utilize the received signal strength indicator (RSSI) to determine the strength of a received signal and hence calculate the distance between itself and the beacon node assuming that the propagation loss between them is known.

After the distance between the sensor node and the beacon nodes are determined based on the methods described above, there remains a need to combine these distance measurements to find the actual location of the sensor node. According to [16], the trilateration and atomic multilateration methods are the two most common ways to combine the distance measurements from three or more beacons. The trilateration and atomic multilateration methods are illustrated in Fig. 9 and described in the following.
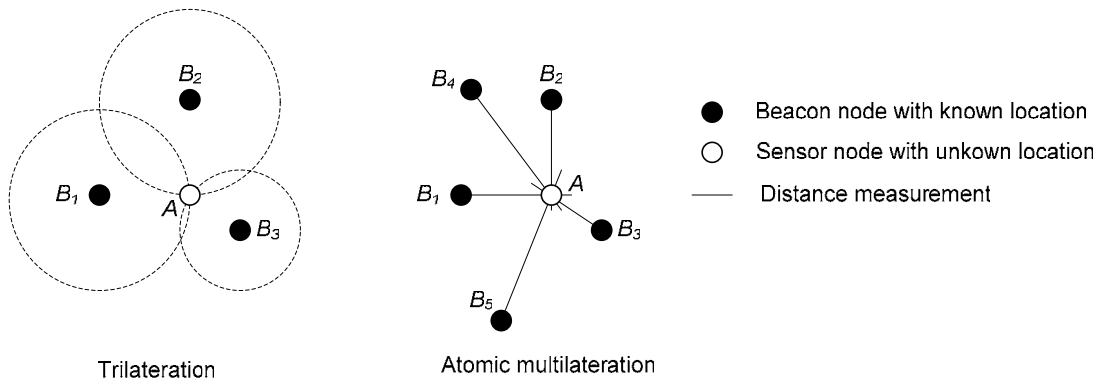
Figure 9.   Trilateration and atomic multilateration for node location discovery (After Ref. [16].).

Trilateration is used when a node has accurate distance measurements between itself and at least three beacon nodes [16]. In Fig. 9, the intersection of the three circles each centered at beacons B_1, B_2 and B_3 gives the location of the sensor node A. How-

ever, this method may not work well if the circles do not intersect at a single point [16]. On the other hand, atomic multilateration uses more than three beacons to discover the location of a sensor node. According to [16], this technique defines an objective function that minimizes the error between the different measured distances by calculating a local minimum of that function. Consider the case in which the exact location of node *A* is denoted by $A(X,Y)$, and the locations of beacon nodes are denoted by $B_1(X_1,Y_1),...,$ $B_K(X_K,Y_K)$. One type of objective function is the sum of residuals as defined by [16]

$$L_1(X,Y) = \sum_{i=1}^{K} |D_i(X,Y) - R_i(X,Y)| \tag{2}$$

where the distance $D_i(X,Y)$ is given by

$$D_i(X,Y) = \sqrt{(X_i - X)^2 + (Y_i - Y)^2} \tag{3}$$

and $R_i(X,Y)$ is the estimated distance between beacon node $B_i(X_i,Y_i)$ and the node $A(X,Y)$. A local minimum of the function given by Equation (2) is computed in order to determine the location of node *A*.

D.   TRANSMISSION RANGE EXTENSION

After the clustering and location discovery functions are accomplished, there remains the question of transmitting the data back to the UAV. As shown in Fig. 6, the role of data transmission is taken up by the primary node in each sensor cluster. However, the limited energy available within the primary node and the omni-directional nature of its antenna radiation pattern may restrict the transmission range between itself and the UAV. Therefore, it is proposed in this thesis to use a sensor cluster to form an array-like transmission to the UAV.

Figure 10 illustrates the potential additional antenna gain G_1 that can be achieved by using a sensor array compared to that of a single sensor node. An additional gain G_2 may be achieved by using more sensor nodes.
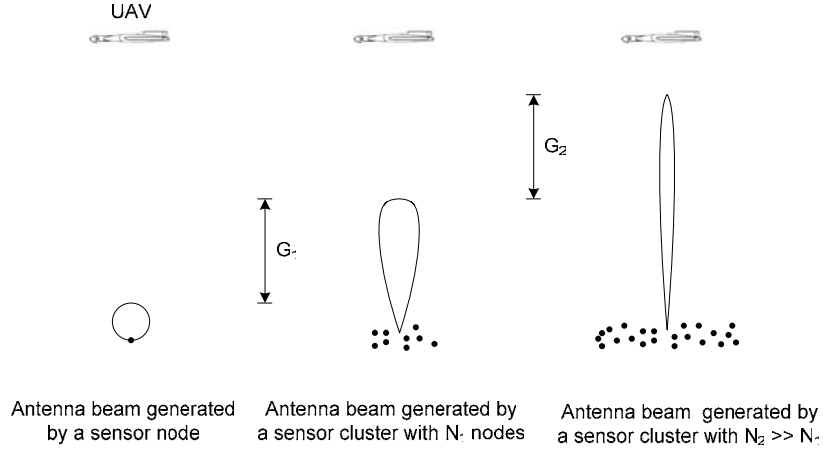
Figure 10.   Higher antenna gain derived from beamforming using sensor cluster.

The free space transmission loss can be expressed as [3]

$$\frac{P_r}{P_t} = \frac{G_t G_r}{L_s} \tag{4}$$

where P_r is the power received by the receiver, P_t is the power transmitted by the transmitter, G_r is the antenna gain of the receiver, G_t is the antenna gain of the transmitter, and L_s is the free space loss given by

$$L_s = \frac{(4\pi R)^2}{\lambda} \tag{5}$$

where R is the transmission range and λ is the free space wavelength. If the sensor cluster and the UAV are represented as transmitter and receiver, respectively, it can be shown in Equation (4) that for fixed P_r/P_t ratio, an increase in G_t by a factor of γ can lead to a reduction in L_s by the same factor. This in turn increases the transmission range R by a factor of $\sqrt{\gamma}$ using Equation (5). Hence, a sensor cluster can be used to form an antenna beam with higher gain to increase the transmission range for data transmission.

15

E.   CHANNEL CAPACITY EXPANSION

The data rate capacity between the sensor nodes and the UAV can be increased by exploiting the multiple-input multiple-output (MIMO) communication nature of the system, which can provide data rate gains [4]. MIMO systems attempt to create multiple transmission channels using several independent mulipaths in a multipath rich environment to increase the channel capacities as compared to a single channel using a transmitting and receiving antenna pair. A basic two-input-two-output narrowband MIMO system is shown in Fig. 11 where four transmission paths exist between the transmitter and the receiver antenna arrays.
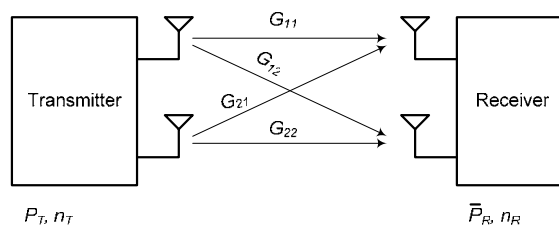
Figure 11.   Two-input-two-output narrowband MIMO system.

Let n_T and n_R be the number of antenna elements at the transmitter and receiver, respectively. The total transmitted power is indicated by P_T, and $\bar{P}_R$ is the average power over all receive elements. The average signal-to-noise ratio at each receiving antenna branch is then given by [4]

$$\rho = \frac{\bar{P}_R}{\sigma^2} \tag{6}$$

where σ^2 is the noise power at each receiving antenna branch.

The channel impulse response matrix $\underset{\sim}{G}$ is given by

$$\underset{\sim}{G} = \begin{bmatrix} G_{11} & G_{12} \\ G_{21} & G_{22} \end{bmatrix} \tag{7}$$

where it is assumed that the channel impulse response is constant over the frequency band of interest, hence the term "narrowband MIMO system". The commonly used normalized channel impulse response matrix is given by

16

$$H = \left(\frac{P_T}{\overline{P}_R} \right) G \qquad (8)$$

and the capacity of the overall MIMO channel C can be represented as the sum of the classical Shannon capacities of each of the spatial channels given by [4]

$$C = \log_2 \det \left[I_{n_R} + \frac{\rho}{n_T} HH^H \right] \qquad (9)$$

where $\det[\bullet]$ represents the determinant and ^{H} represents the conjugate transposition. Let λ_k represent the eigenvalues of HH^H. In the case of the two-input-two-output narrowband MIMO system, Equation (9) is equivalent to the following [4]

$$C = \sum_{k=1}^{2} \log_2 \left[1 + \frac{\rho}{n_T} \lambda_k \right] \qquad (10)$$

which is simplified to become

$$C = \log_2 \left[1 + \frac{\rho}{2} \lambda_1 \right] + \log_2 \left[1 + \frac{\rho}{2} \lambda_2 \right]. \qquad (11)$$

Assuming that the channel is lossless and all eigenvalues are the same, it can be shown in Equation (11) that the channel capacity increases by a factor of two. Figure 12 shows a general n_T-input-n_R-output narrowband MIMO system with the normalized channel impulse response given by H_{ij}. Considering the increased number of transmission multipaths between the transmitter and receiver as shown in Fig.12, Equation (10) can be extended so that the capacity C becomes

$$C = \sum_{k=1}^{K} \log_2 \left[1 + \frac{\rho}{n_T} \lambda_k \right] \qquad (12)$$

where K is $\min[n_T, n_R]$. Therefore, the channel capacity can be increased to several orders of magnitude by increasing n_T and n_R, as indicated by Equation (12).
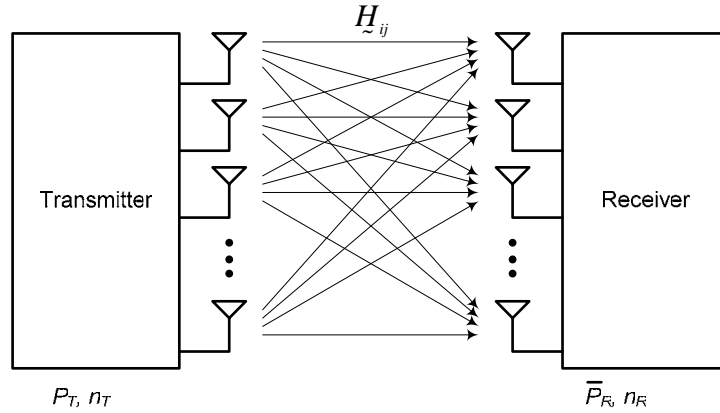
Figure 12.   A MIMO narrowband system with n_T inputs and n_R outputs.

The sensor nodes may be deployed over an area where a large number of communication transmission multipaths exist due to the presence of man-made structures or natural obstacles. Figure 13 illustrates how the sensor cluster and the UAV can be considered a type of MIMO system consisting of multi-element array elements at both ends of the communication link. Multiple channels are created using several independent multipaths in the multipath rich environment to increase the channel capacities. Such a system could offer a unique solution for supporting large bandwidth requirements in future military applications.
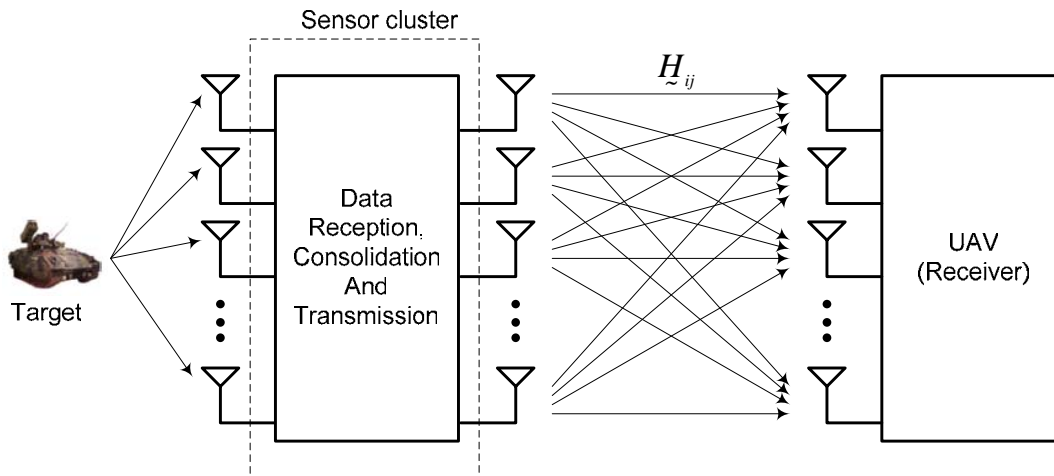
Figure 13.   Sensor cluster as part of MIMO system.

18

F. SUMMARY

In this chapter, various WSN architectures were discussed, and a hierarchical three-tier architecture is proposed for use in this thesis. This was followed by the discussion of some common clustering and location discovery methods for WSNs. The advantages of using sensor cluster to increase the transmission range and/or channel capacity between the sensor nodes and the UAV were also described. The next chapter will discuss the fundamental concepts required for each sensor cluster to form an array-like transmission to the UAV.

THIS PAGE INTENTIONALLY LEFT BLANK

III. SENSOR CLUSTER AND BEAMFORMING

After the sensor nodes are deployed by the UAV, they are grouped into clusters, and a primary node is elected from among the sensor nodes within a cluster using the methods described in Chapter II, Section B. The location of the sensor nodes can be determined using techniques presented in Chapter II, Section C. Distributed beamforming is then initiated and coordinated by each primary node within the cluster in order to increase the transmission range and/or channel capacity between each cluster and the UAV.

This chapter presents the fundamental concepts required for each sensor cluster to form an array-like transmission to the UAV. In particular, it discusses the array factor and power gain of antenna arrays and random arrays. The adaptive beamforming scheme is also described. This is followed by the discussion of various algorithms that can estimate the AOA and track the desired signal using passive arrays. Lastly, it also discusses the significance of the antenna beamwidth for UAV detection and tracking.

A. ONE-DIMENSIONAL ARRAY

Figure 14 shows an $M \times 1$ omni-directional antenna array located in the far field of a point source (e.g., an UAV). The point source emits a signal that consists of a complex signal $s(t)$ modulating a carrier $e^{j\omega_c t}$. The plane wavefront arrives at an elevation angle θ_0 with respect to the array normal (i.e., z-axis). For convenience, the reference is taken at the origin, and it is assumed that the wavefront arrives at the mth element t_m seconds before it reaches the origin. Hence, the signal arriving at the mth element leads the signal arriving at the origin by [5]

$$t_m(\theta_0) = \frac{x_m \sin \theta_0}{c} \tag{13}$$

where c is the speed of light and x_m is the x-coordinate of the mth element.
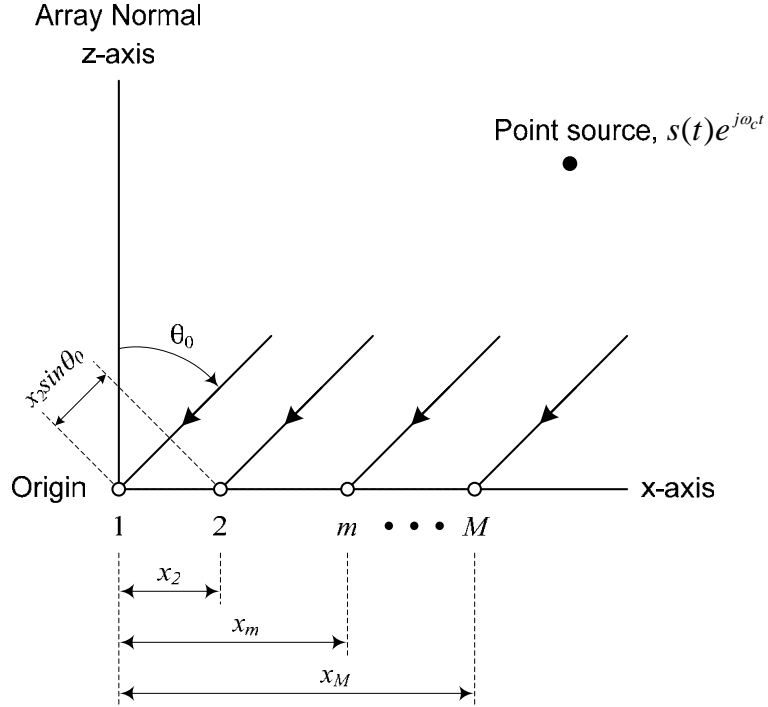
Figure 14.   An $M \times 1$ omni-directional antenna array.

It can be seen from Equation (13) that $t_m(\theta_0)$ is determined by the AOA of the desired signal indicated by θ_0 and the element's position indicated by x_m. For any arbitrary angle θ, the signal arriving at the mth element leads the signal arriving at the origin by

$$t_m(\theta) = \frac{x_m \sin \theta}{c}. \qquad (14)$$

Without considering the effects of mutual coupling among the array elements, the spatial response (or array factor) of the array is obtained by adding all the array element outputs together giving [18]

$$F(\theta) = \sum_{m=1}^{M} I_m e^{-j\omega_c t_m(\theta_0)} e^{j\omega_c t_m(\theta)} \qquad (15)$$

where I_m and $e^{-j\omega_c t_m(\theta_0)}$ are the magnitude and phase of the current induced on the mth element. Together, I_m and $e^{-j\omega_c t_m(\theta_0)}$ form what is commonly known as the complex weights. Notice that the phase reversal in the term $e^{-j\omega_c t_m(\theta_0)}$ is required in order to create a maximum value of $F(\theta)$ at $\theta = \theta_0$. Hence, the maximum value of $F(\theta)$ occurs at

22

$\theta = \theta_0$ and the main lobe points towards θ_0. Equation (15) can be written in the form given by [18]

$$F(\theta) = \sum_{m=1}^{M} I_m e^{-j\beta(x_m \sin \theta_0)} e^{j\beta(x_m \sin \theta)} \tag{16}$$

where β is the wavenumber given by $2\pi / \lambda$ and λ is the wavelength, and can be compactly expressed as

$$F(\theta) = \sum_{m=1}^{M} w_m^* e^{j\beta(x_m \sin \theta)} \tag{17}$$

where $w_m = I_m e^{j\beta(x_m \sin \theta_0)}$ is the complex weight applied to the mth element. The far-field beam pattern (or power gain) is given by

$$G(\theta) = |F(\theta)|^2. \tag{18}$$

Consider an $M \times 1$ uniformly excited unit array (i.e., equal current magnitude of 1) consisting of isotropic elements (i.e., antennas with omni-directional radiation pattern) and with the main lobe pointing at $\theta_0 = 0°$. The maximum array factor is computed to be

$$F(\theta_0) = \sum_{m=1}^{M} w_m^* e^{j\beta(x_m \sin \theta)} = \sum_{m=1}^{M} I_m e^{-j\beta(x_m \sin \theta_0)} e^{j\beta(x_m \sin \theta_0)} = \sum_{m=1}^{M} 1 = M$$

using Equation (17) while the power gain is calculated to be M^2 using Equation (18). Therefore, the power gain of a uniform array can be increased by increasing the number of elements. This implies that more sensor nodes can be used within a sensor cluster to produce an antenna beam with higher power gain and hence increase the transmission range between the sensor cluster and the UAV, which was described earlier in Chapter II, Section D.1.

The plot of the normalized power gain G_n (in dB) versus θ (in degrees) is shown in Fig. 15 to illustrate the main characteristics of the antenna beam generated by a 10×1 uniformly excited array. The array consists of isotropic elements with fixed element-element spacing $d = \lambda/2$, and the main lobe is assumed to point at $\theta_0 = 0°$ Figure 15(a) shows that the main lobe points in a direction perpendicular to the array axis (i.e., x-axis) and can be categorized as a broadside radiation pattern. As shown in Fig. 15(b), the 3-dB

23
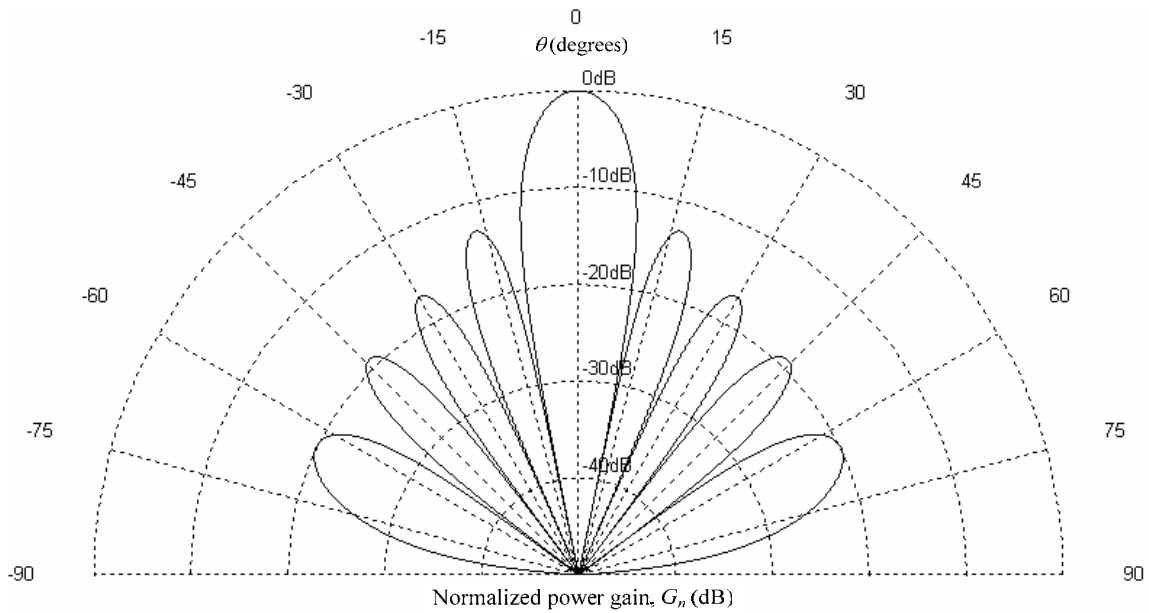
(a)
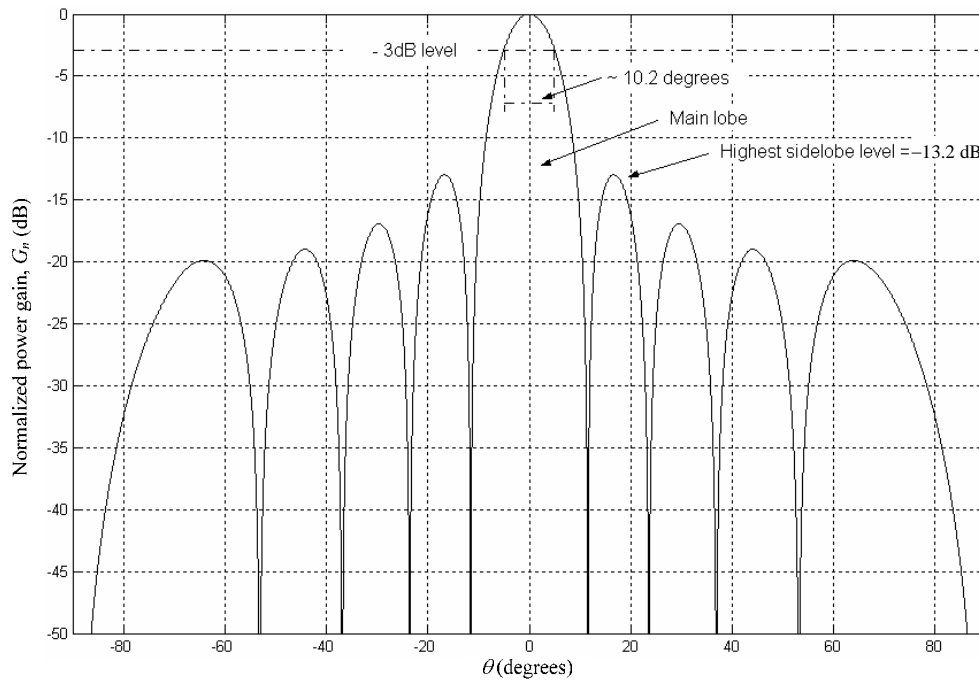
(b)

Figure 15.   Normalized power gain of the beam generated by a 10×1 uniformly excited square array with isotropic elements, fixed element spacing of $d = \lambda/2$, and $\theta_0 = 0°$: (a) Polar plot and (b) X-Y plot indicating the 3-dB beamwidth of 10.2° and the highest sidelobe level of -13.2 dB.

(or half power) beamwidth θ_{3dB} is about $10.2°$, and the highest sidelobe level $S_{L\max}$ is about 13.2 dB below the main lobe level.

The 3-dB beamwidth of a uniformly excited broadside array (i.e., $\theta_0 = 0°$) with isotropic elements and fixed element spacing is given by [18]

$$\theta_{3dB} \approx 0.866 \frac{\lambda}{Md} \tag{19}$$

where a long $(i.e., Md \gg \lambda)$ array has been assumed. The 3-dB beamwidth is calculated to be $9.92°$ using Equation (19), showing reasonable agreement with the $10.2°$ obtained from the plot. It can be seen from Equation (19) that θ_{3dB} can be controlled by adjusting M. For example, when M is increased by a factor of γ, θ_{3dB} is reduced by the same factor, resulting in a narrower beam and vice versa. This allows θ_{3dB} to be adjusted by changing the number of sensor nodes required for beamforming during the detection and tracking of UAV. For example, a large θ_{3dB} is usually required to create a large detection region while a small θ_{3dB} is preferred to obtain the required tracking resolution of the UAV. This is further discussed in Section G.2 later in this chapter.

The array factor and the power gain of a one-dimensional array can be extended to a two-dimensional array as presented in the next section.

B.   TWO-DIMNESIONAL ARRAY

Figure 16 shows an $M \times N$ omni-directional antenna array located in the far field of a point source. The plane wavefront arrives at an elevation angle θ_0 with respect to the z-axis and an azimuth angle of ϕ_0 with respect to the x-axis. The reference is taken at the origin, and it is assumed that the wavefront arrives at the $(m,n)^{th}$ element t_{mn} seconds before it reaches the origin. Therefore, the signal arriving at the $(m,n)^{th}$ element leads the signal arriving at the origin by [5]

$$t_{mn}(\theta_0,\phi_0) = \frac{x_{mn} \sin\theta_0 \cos\phi_0 + y_{mn} \sin\theta_0 \sin\phi_0}{c} \tag{20}$$

where c is the speed of light and (x_{mn}, y_{mn}) is the x-coordinate and y-coordinate of the $(m,n)^{th}$ element.
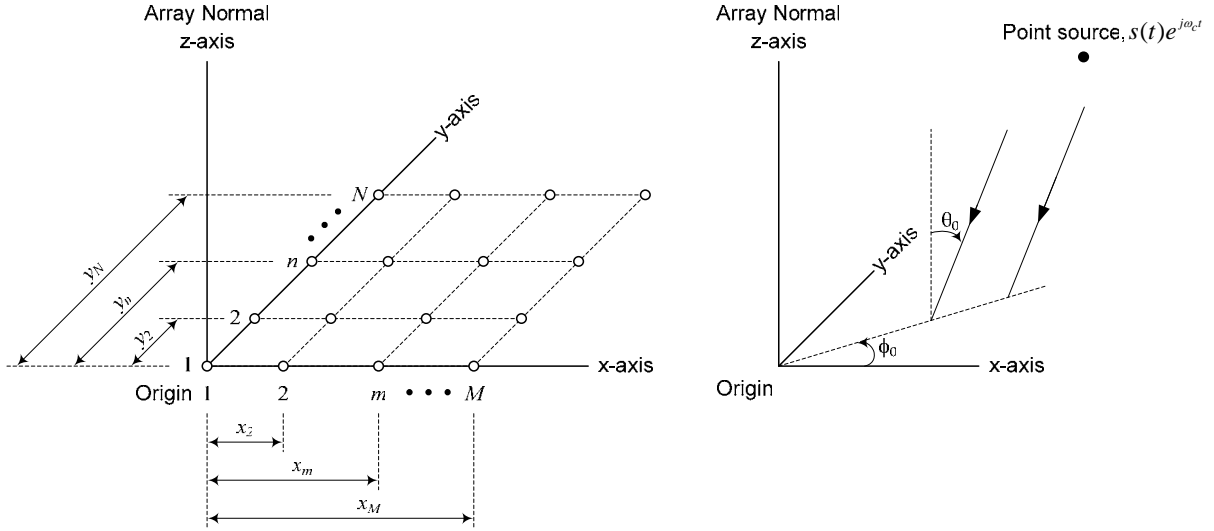
Figure 16.   An $M \times N$ omni-directional antenna array.

For any set of arbitrary angles, (θ, ϕ), the signal arriving at the $(m,n)^{th}$ element leads the signal arriving at the origin by

$$t_{mn}(\theta, \phi) = \frac{x_{mn} \sin \theta \cos \phi + y_{mn} \sin \theta \sin \phi}{c}.$$
(21)

The two-dimensional array factor $F(\theta, \phi)$ is given by [18]

$$F(\theta, \phi) \;\; = \sum_{m=1}^{M} \sum_{n=1}^{N} I_{mn} e^{-j\beta(x_{mn} \sin \theta_0 \cos \phi_0 + y_{mn} \sin \theta_0 \sin \phi_0)} e^{j\beta(x_{mn} \sin \theta \cos \phi + y_{mn} \sin \theta \sin \phi)}$$
(22)

without considering the effects of mutual coupling among the array elements. Equation (22) can be rewritten as

$$F(\theta, \phi) = \sum_{m=1}^{M} \sum_{n=1}^{N} w_{mn}^{*} e^{j\beta(x_{mn} \sin \theta \cos \phi + y_{mn} \sin \theta \sin \phi)}$$
(23)

where β is the wavenumber given by $2\pi / \lambda$, and $w_{mn} = I_{mn} e^{j\beta(x_{mn} \sin \theta_0 \cos \phi_0 + y_{mn} \sin \theta_0 \sin \phi_0)}$ is the complex weight applied to the $(m,n)^{th}$ element. The maximum value of $F(\theta, \phi)$ occurs

26

at $(\theta,\phi) = (\theta_0,\phi_0)$, and the main lobe points towards (θ_0,ϕ_0). The power gain is defined as

$$G(\theta,\phi) = |F(\theta,\phi)|^2 . \qquad (24)$$

Consider an $M \times N$ uniformly excited array with isotropic elements and the main lobe pointing at $\theta_0 = \phi_0 = 0°$. The maximum array factor and the power gain are NM and $(NM)^2$, respectively. Similar to the one-dimensional case, the power gain of a two dimensional uniform array can be increased by increasing the number of elements.

The beam pattern formed by 3×3, 5×5 and 7×7 arrays are shown in Fig. 17 in which plots were generated for $\phi = 45°$. These uniformly excited square arrays consist of isotropic elements with a fixed element-element spacing $d = \lambda/2$. The main lobe for all the three arrays is assumed to point at $(\theta_0,\phi_0) = (0°,45°)$ as illustrated in Fig. 17(a). Figure 17(b) shows that θ_{3dB} increases from $15°$ to $37°$ when the number of array elements decreases from 7×7 to 3×3. Therefore, the antenna beam of a uniformly excited array with isotropic elements and fixed element-element spacing becomes broader when the number of elements decreases. This observation is consistent with that concluded in the previous section for the one-dimensional case.

(a)

(b)
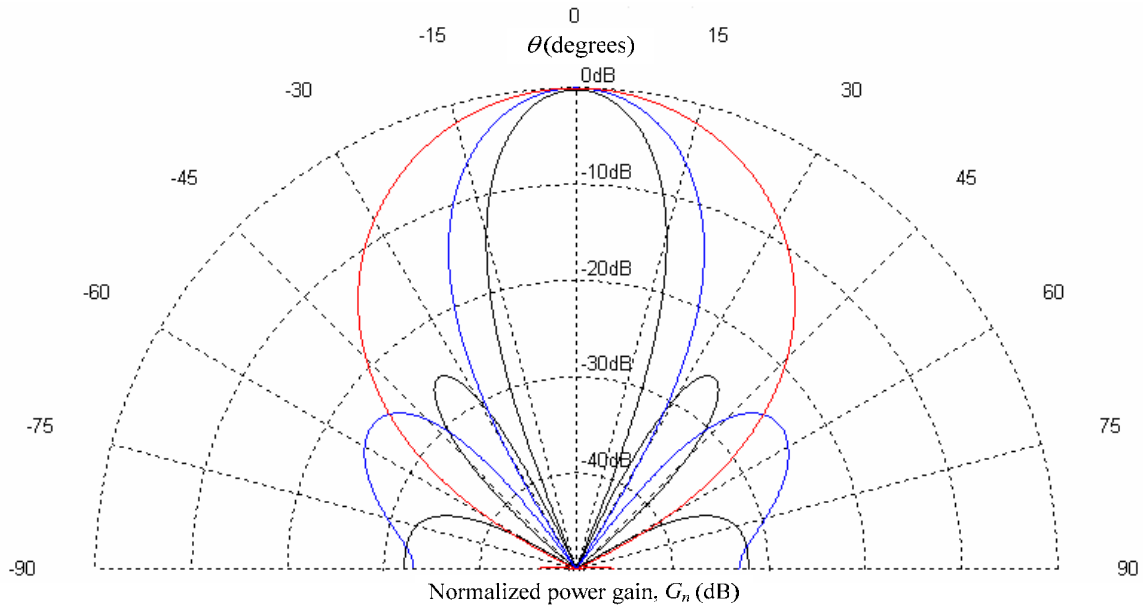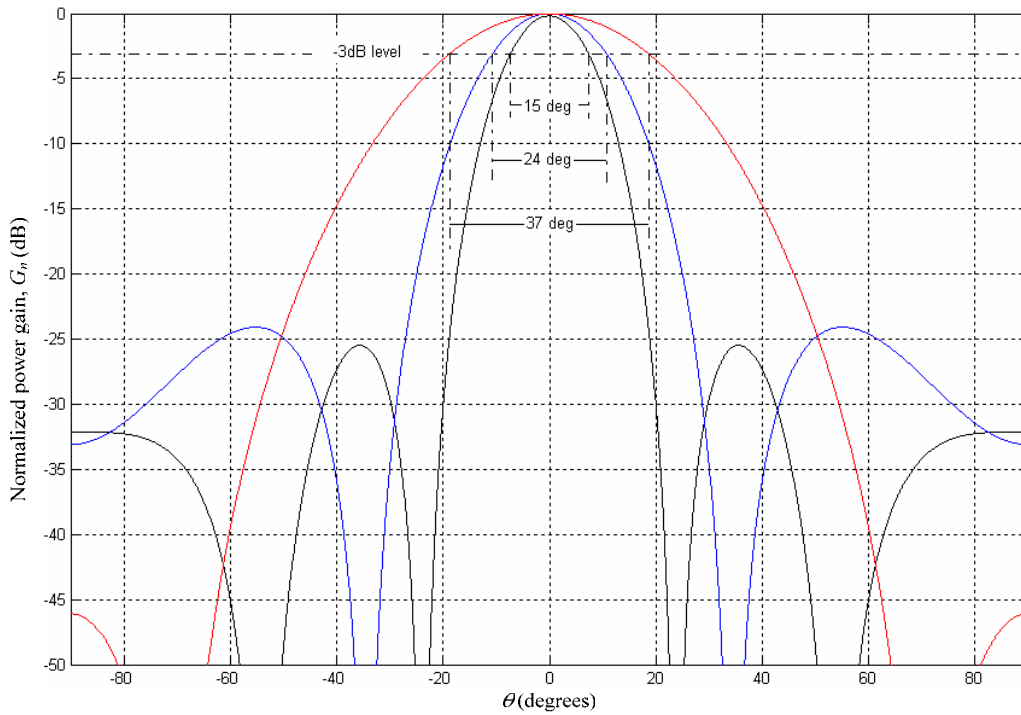
Figure 17.   Normalized power gain of the beams generated by 7×7, 5×5 and 3×3 uniformly
excited square arrays with isotropic elements, fixed element spacing of $d = \lambda/2$, and
$(\theta_0, \phi_0) = (0°, 45°)$: (a) Polar plots and (b) X-Y plots showing the decrease in 3-dB beam-
width as the number of elements increase.

In summary, the array factor and power gain equations for the two-dimensional array were presented in this section, and it was concluded that they were affected by the AOA of the desired signal, the number of array elements, array element positions, and the complex weights w_{mn}. The main characteristics of the antenna beam, such as 3-dB beamwidth and highest sidelobe level, were introduced. The effects of the number of array elements on the antenna power gain and the 3-dB beamwidth were also discussed.

C.   RANDOM ARRAY

Sensor nodes are deployed randomly over an area of interest, resulting in random positioning of the sensor nodes. Subsequently, these sensor nodes form clusters using methods described in Chapter II, Section B and their locations are determined using location discovery techniques presented in Chapter II, Section C. The random position of the sensor nodes within the sensor cluster gives rise to what is referred to as random arrays. This section discusses the theoretical findings related to random arrays, positioning error and element failures in antenna arrays.

1.   Average Power Gain

The average power gain of one dimensional $M \times 1$ random array is given by [7]

$$\overline{G}(\theta) = \overline{|F(\theta)|^2} = G_o(\theta)\left(1 - \frac{1}{M}\right) + \left(\frac{1}{M}\right) \tag{25}$$

where $G_o(\theta)$ is the designed power gain and M is the number of array elements.

The first term $G_o(\theta)\left(1 - \frac{1}{M}\right)$ is an angle-dependent term, which shows that $G_o(\theta)$ is reduced depending on the number of array elements M. For example M must decrease from 100 to 2 in order to produce a 3-dB reduction in $G_0(\theta)$. The second term $\left(\frac{1}{M}\right)$ is an angle-independent, additive term and relates to the power ratio of the average sidelobe to the main lobe. For example, the average sidelobe level is computed to be -20 dB when $M = 100$ and -3 dB when $M = 2$, an increment of 17 dB. It can be seen

that increasing the number of array elements can help reduce the loss in the average power gain and decrease the average sidelobe level, even though the latter is more sensitive to the number of elements than the average power gain. It was further suggested in [7] that the shape of the main lobe is also not significantly affected by the random positions of the array elements.

2. Position Errors

Reference [8] considered the presence of both amplitude and phase errors in a two-dimensional $M \times N$ array with equal weights, i.e., $I_{mn} = I$. The expected value of the increase in sidelobe level Δs, relative to the main lobe, is given by

$$\Delta s = \frac{1}{MN} \left[\frac{1}{e^{-\sigma_{\Delta p}^2}} \left(1 + \frac{\sigma_{\Delta a}^2}{I^2} \right) - 1 \right] \tag{26}$$

where $\sigma_{\Delta a}^2$ is the variance of the amplitude error in volts^2 and $\sigma_{\Delta p}^2$ is the variance of the phase error in rad^2, assuming gaussian phase errors.

Considering only the presence of phase errors, it can be calculated, using Equation (26), that the sidelobe level increases about 6 dB when $\sigma_{\Delta p}$ increases by a factor of two. For example, assuming that $MN = 9$, Δs is calculated to be 0.0034 when $\sigma_{\Delta p} = 10°$ and $\Delta s = 0.014$ when $\sigma_{\Delta p} = 20°$, an increment of about 6 dB caused by an increase in the phase error by a factor of two.

It is also noted from Equation (26) that the amount of increase in the sidelobe level can be reduced by using more array elements indicated by the MN term in the denominator. It can be shown that it takes the number of array elements to increase by a factor of two in order to reduce Δs by 3 dB.

The fractional loss L_p in the main lobe gain for a two-dimensional $M \times N$ array with equal weights is given by [8]

$$L_p = e^{-\sigma_{\Delta p}^2} \tag{27}$$

where $\sigma_{\Delta p}^2$ is the variance of the phase error, assuming gaussian phase errors. It can be calculated, using Equation (27), that a phase error of $\pm 47°$ is required to cause a 3-dB re-

30

duction in the main lobe gain. This suggests that a large position error is required to reduce the main lobe gain by 3 dB.

3.   Element Failures

The fractional loss L_f in the main lobe gain for a two-dimensional $M \times N$ array with equal weights due to element failures is given by [8]

$$L_f = \left(\frac{M'N'}{MN} \right)^2 \tag{28}$$

where $M'N'$ is the number of operating elements and MN is the total number of elements. Since element failures are random, the operating probability of any element p_0 is given by

$$p_0 = \lim_{MN \to \infty} \frac{M'N'}{MN}. \tag{29}$$

Hence, the expected value of the main lobe gain, relative to error-free array, is reduced by a factor of p_0^2.

In summary, this section has developed some insights into the effects of random positions of array elements, random position errors and element failures on the antenna beam characteristics. Some important conclusions can be made as follows:

1. The average power gain of the main lobe is not significantly affected by random positions or position errors of the array elements. The shape of the main lobe is also not significantly affected by the random positions of the array elements.

2. Sidelobe levels are affected by random positions or position errors of the array elements, and a lower sidelobe level is likely to be maintained when the number of array elements is large.

3. The loss in the main lobe power gain is proportional to the square of the probability of the element being operative.

After the fundamental ideas of two dimensional arrays and random arrays were presented, the next section describes the array beamforming processing which is required to form a directed antenna beam towards the UAV.

D.   BEAMFORMING

It was concluded in Section B of this chapter that the array factor is affected by the AOA of the desired signal, the number of array elements, array element positions, and the complex weights w_{mn}. An array beamformer works by adjusting the magnitudes and/or phases of the complex weights w_{mn} and steers the main lobe towards the desired direction, assuming that the AOA of desired signal, the number of array elements and positions of the array elements are known. In a WSN, the positions of the sensor nodes can be obtained by methods described in Chapter II, Section C while methods to estimate and track the AOA of the desired signal are described in Section F of this chapter. This section starts by discussing some of the common array beamformers found in [17] before presenting the type of beamformer selected for this thesis.

According to [17], a conventional beamformer is a delay-and-sum beamformer with complex weights of equal magnitudes. The phases are selected so as to steer the beam in the desired direction. Another type of beamformer called the null-steering beamformer adjusts the complex weights so as to produce a null in the array factor in the direction of the interference signal. An optimal beamformer computes the complex weights so that the main lobe has the highest signal-to-noise ratio. A narrowband beamformer is basically a combination of the conventional and null-steering beamformers. It uses a known reference signal (which is closely correlated to the desired signal) to estimate the complex weights by subtracting the array output from this reference signal and computing the error. The complex weights are then adjusted so as to minimize the mean square error. This type of beamformer has the ability to steer the beam in the desired direction and create nulls in the direction of the interfering signals. As such, the narrowband beamformer is used in this thesis.

Consider an $M \times N$ omni-directional antenna array shown in Fig. 18. Recall from Fig. 16 that the point source emits a signal that consists of a complex modulating signal $s(t)$ modulated by a carrier $e^{j\omega_c t}$. The signal received at the $(m,n)^{\text{th}}$ element at time t is given by

$$X_{mn}(t) = s\left(t + t_{mn}\left(\theta_0, \phi_0\right)\right) e^{j\omega_c\left(t + t_{mn}(\theta_0, \phi_0)\right)} + n_{mn}(t) \tag{30}$$

where $t_{mn}(\theta_0, \phi_0)$ represents the signal time lead at the $(m, n)^{\text{th}}$ element with respect to the origin and $n_{mn}(t)$ is white noise with zero mean and variance of σ_n^2. As shown in Fig. 18, the complex weights w_{mn}, which were introduced in Section B, are applied to the signal received by the array elements and summed together to give the beamformer output.
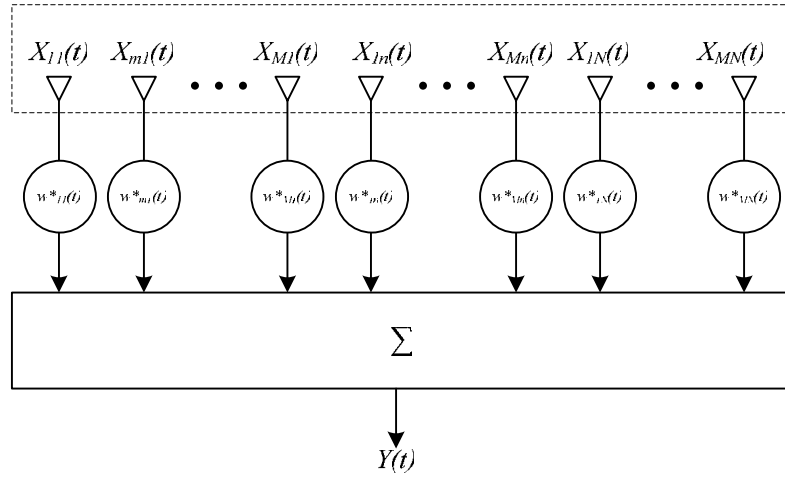
Figure 18. $M \times N$ narrow-band beamformer.

Generally, $s(t)$ is assumed to be a narrow-band signal and hence satisfies the following condition given by [19]

$$B_m \Delta T_{\max} << 1 \tag{31}$$

where B_m is the bandwidth of $s(t)$ and $\Delta T_{\max}$ is the maximum travel time of $s(t)$ between two successive elements in the array. In most cases, the bandwidth of $s(t)$ and the dimensions of the array are small enough so that this condition is satisfied. Therefore, $s(t)$ remains constant during the $t_{mn}(\theta_0, \phi_0)$ seconds and the approximation $s(t + t_{mn}(\theta_0, \phi_0))$ $\approx s(t)$ holds. In addition, the carrier term $e^{j\omega_c t}$ can be removed since the phase delay experienced by the carrier, $e^{j\omega_c t_{mn}(\theta_0, \phi_0)}$, is of interest. The signals received at the $(m, n)^{\text{th}}$ element then becomes

$$X_{mn}(t) = s(t)e^{j\omega_c t_{mn}(\theta_0, \phi_0)} + n_{mn}(t) \tag{32}$$

33

and can be rewritten in vector form given by:

$$\underline{X}(t) = s(t)\underline{v} + \underline{n}(t) \tag{33}$$

where $\underline{v}$ is the steering vector associated with the direction (θ_0, ϕ_0) of the desired signal and $\underline{n}(t)$ is noise vector. The steering vector $\underline{v}$ contains the AOA information and is represented as a one-dimensional $MN \times 1$ vector given by

$$\underline{v} = [e^{j\omega_c t_{11}(\theta_0, \phi_0)}, \ \ldots \ , \ e^{j\omega_c t_{M1}(\theta_0, \phi_0)}, \ e^{j\omega_c t_{1n}(\theta_0, \phi_0)}, \ \ldots \ , \ e^{j\omega_c t_{Mn}(\theta_0, \phi_0)}, \ e^{j\omega_c t_{1N}(\theta_0, \phi_0)}, \ \ldots \ , \ e^{j\omega_c t_{MN}(\theta_0, \phi_0)}]^T \tag{34}$$

where ^{T} represents the matrix transposition. The noise vector $\underline{n}(t)$ is written as a one dimensional $MN \times 1$ vector given by

$$\underline{n}(t) = [n_{11}(t), \ n_{m1}(t), \ \ldots \ , \ n_{M1}(t), \ n_{1n}(t), \ \ldots \ , \ n_{Mn}(t), \ n_{1N}(t), \ \ldots \ , \ n_{MN}(t)]^T. \tag{35}$$

The beamformer output $Y(t)$ can be written as

$$Y(t) = \underline{w}^* \underline{X}(t) \tag{36}$$

where * represents the complex conjugate operation, $\underline{w}^*$ is a one-dimensional $1 \times MN$ vector given by

$$\underline{w}^*(t) = [\underline{w}_{11}^*(t), \ \underline{w}_{m1}^*(t), \ \ldots \ , \ \underline{w}_{M1}^*(t), \ \underline{w}_{1n}^*(t), \ \ldots \ , \ \underline{w}_{Mn}^*(t), \ \underline{w}_{1N}^*(t), \ \ldots \ , \ \underline{w}_{MN}^*(t)] \tag{37}$$

and $\underline{X}(t)$ is an $MN \times 1$ vector given by

$$\underline{X}(t) = [X_{11}(t), \ X_{m1}(t), \ \ldots \ , \ X_{M1}(t), \ X_{1n}(t), \ \ldots \ , \ X_{Mn}(t), \ X_{1N}(t), \ \ldots \ , \ X_{MN}(t)]^T. \tag{38}$$

The complex weights $\underline{w}$ are chosen in order to create a maximum array factor at $\theta = \theta_0$ and $\phi = \phi_0$ given by Equation (23). Hence, the narrow-band beamformer in Fig. 18 provides a means to create a maximum array factor in the desired direction by selecting the appropriate complex weights. This works well when the AOA is fixed. In cases when the point source is mobile (e.g., an UAV), the AOA changes and an adaptive beamformer is required, which is presented in the next section.

E.   ADAPTIVE BEAMFORMING

The AOA changes when the point source is moving and an adaptive beamformer is required to steer the main lobe towards the point source when the latter is mobile.

Various adaptive algorithms exist, such as the least mean squares (LMS), recursive least squares (RLS) and constant modulus algorithm (CMA). Both the LMS and RLS algorithms require knowledge of the desired signal $s(t)$ (or something closely correlated to it), while the CMA is a blind adaptive algorithm, which requires no knowledge of the desired signal. The LMS algorithm is based on the steepest-descent optimization method that recursively computes and updates the complex weights. It is the most common adaptive algorithm for continuous adaptation and has been well studied and is well understood [8]. In this thesis, the LMS algorithm is selected for the adaptive beamforming process due to its simplicity.

Figure 19 shows the block diagram of a narrow-band adaptive beamformer using the LMS algorithm. It can be used to steer the main beam towards the point source while simultaneously suppressing interfering signals through adjustment of the complex weights.
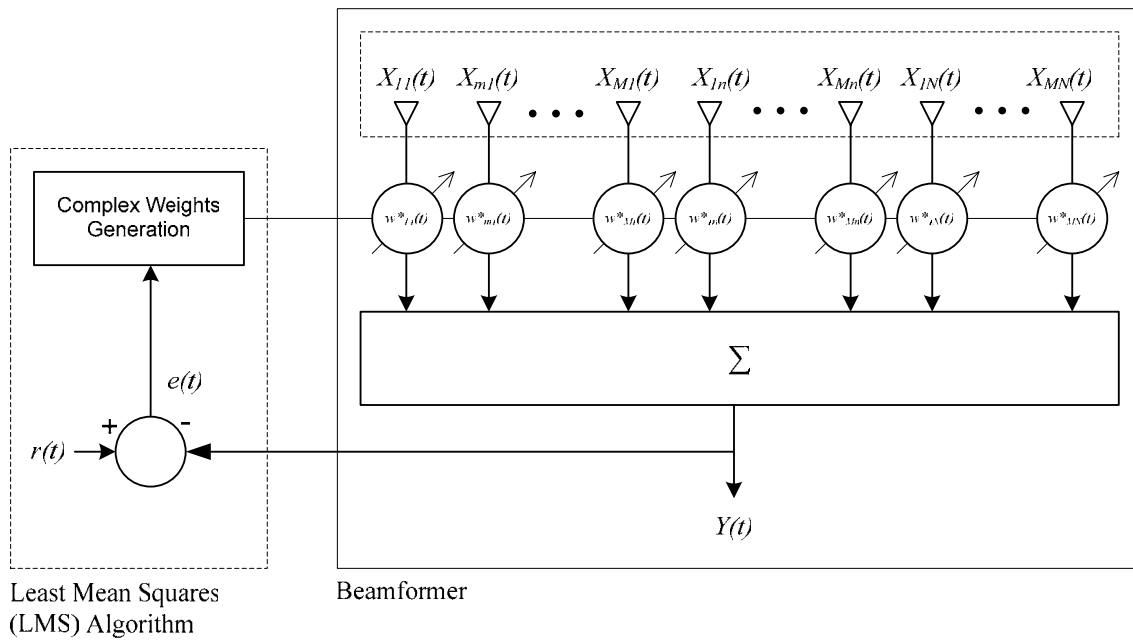
Figure 19. $M \times N$ narrow-band adaptive beamformer.

The error $e(t)$ is defined to be:

$$e(t) = r(t) - Y(t) \tag{39}$$

35

where $r(t)$ is the reference signal and $Y(t)$ is the output of the beamformer. In practice, $r(t)$ needs to be closely correlated to the desired signal $s(t)$.

The complex weights are adjusted and applied to the signal received by the array elements in an iterative manner. For each iteration, the complex weights are chosen to minimize the mean-square error between the beamformer output $Y(t)$ and the reference signal $r(t)$ given by [8]

$$E\left[e^2(t)\right] = E\left[\left(r(t) - Y(t)\right)^2\right] \tag{40}$$

which can be expanded to the form given by

$$E\left[e^2(t)\right] = E\left[r^2(t)\right] - 2\underline{w}^H E\left[r(t)\underline{X}(t)\right] + \underline{w}^H E\left[\underline{X}(t)\underline{X}^H(t)\right]\underline{w}, \tag{41}$$

where $E[\bullet]$ is the expectation operator. The minimum mean-square error (MMSE) is obtained by setting the gradient vector of Equation (41) with respect to $\underline{w}$ to zero, giving

$$\nabla_{\underline{w}} E\left[e^2(t)\right] = -2E\left[r(t)\underline{X}(t)\right] + 2E\left[\underline{X}(t)\underline{X}^H(t)\right]\underline{w}. \tag{42}$$

According to the method of steepest descent, the value of the weight vector at time $(t+1)$ is updated as follows

$$\underline{w}(t+1) = \underline{w}(t) + \frac{1}{2}\mu\left[-\nabla_{\underline{w}} E\left[e^2(t)\right]\right] \tag{43}$$

where μ is the convergence factor. By substituting $\nabla_{\underline{w}} E\left[e^2(t)\right]$ from Equation (42) into the above equation, we have

$$\begin{aligned}
\underline{w}(t+1) &= \underline{w}(t) + \frac{1}{2}\mu\left[2E\left[r(t)\underline{X}(t)\right] - 2E\left[\underline{X}(t)\underline{X}^H(t)\right]\underline{w}\right] \\
&= \underline{w}(t) + \mu\left[r(t)\underline{X}(t) - \underline{X}(t)\underline{X}^H(t)\underline{w}\right] \\
&= \underline{w}(t) + \mu\underline{X}(t)\left[r(t) - \underline{X}^H(t)\underline{w}\right]
\end{aligned}$$

which can be simplified to become:

$$\underline{w}(t+1) = \underline{w}(t) + \mu\underline{X}(t)e^*(t) \tag{44}$$

where * represents complex conjugation and the instantaneous estimates given by $\left[r(t) \underline{X}(t) \right]$ and $\left[\underline{X}(t) \underline{X}^H(t) \right]$ have been used instead of $E\left[r(t) \underline{X}(t) \right]$ and $E\left[\underline{X}(t) \underline{X}^H(t) \right]$, respectively. The term $E\left[\underline{X}(t) \underline{X}^H(t) \right]$ is commonly known as the array correlation matrix R and denotes the correlation between the signals received by the various array elements. The convergence factor μ is related to the eigenvalues of $\underline{X}\underline{X}^H$. If the eigenvalues of $\underline{X}\underline{X}^H$ are widely spread, convergence will be slow. For convergence of the LMS algorithm, the value of μ needs to be in the range given by [20]

$$0 < \mu < 2 / \lambda_{max} \tag{45}$$

where λ_{max} is the maximum eigenvalue of $\underline{X}\underline{X}^H$.

The narrow-band adaptive beamformer presented can be used to beamform and steer the main beam of the array towards the mobile point source. However, knowledge about the AOA of the desired signal is a prerequisite for the beamforming process. As such, methods of determining the AOA of the desired signal are presented in the next section.

F.   AOA ESTIMATION AND TRACKING

The knowledge about the AOA of the desired signal is a prerequisite for the beamforming process. Although it is not the focus of this thesis to provide an in-depth study of existing AOA estimation and tracking methods, they are briefly introduced in this section for completeness. The intention is to provide an overview of the common AOA estimation techniques as summarized by [17]. Methods to track the estimated AOA are also discussed.

1.   Spectral Estimation Methods

Spectral estimation methods estimate the AOA by analyzing the spatial spectrum and then determining the local maxima. According to [17], one of the earliest methods is the Barlett method which applies equal weighting on each array element and estimates the mean input power. The direction that gives the highest mean power is the AOA of the desired signal source. The antenna beamwidth needs to be very narrow and the sidelobe levels need to be low with respect to the main lobe in order for this method to

work well. This is because the input power is contributed from both the main lobe and the sidelobes of the beam. A high sidelobe level may mislead the algorithm in deducing that the AOA of the source is in the direction in which the sidelobe is pointing and not the direction in which the main lobe is pointing.

Another spectral analysis method is the minimum-variance distortionless response (MVDR), which finds the maximum likelihood estimate of the power arriving from a point source in direction θ_0 assuming all other sources as interferences. The array weights are adjusted to cancel the interference signals and maintain a unity power gain at θ_0.

2.   Linear Prediction Method

This method estimates the output of one sensor using linear combinations of the remaining sensor outputs and minimizes the mean square prediction error, which is the error between the estimated and actual output. It obtains the array weights by minimizing the mean output power of the array subject to the constraint that the weight on the selected array element is unity.

3.   Multiple Signal Classification (MUSIC)

MUSIC is a type of eigenstructure method that relies on the properties of the array correlation matrix R. The space spanned by the eigenvectors of R may be partitioned into a signal subspace and a noise subspace [17]. The steering vectors corresponding to the directional sources are orthogonal to the noise subspace and are found within the signal subspace. Several variations of MUSIC exists, but in its standard form, the method estimates the noise subspace from the samples collected at the array elements. Once the noise subspace has been estimated, a search for AOA of the desired signal is made by looking for steering vectors that are as orthogonal to the noise subspace as possible.

4.   Estimation of Signal Parameters via Rotational Invariant Techniques (ESPRIT)

This method requires two arrays with identical element displacement vectors. In other words, the elements in the first array are displaced by the same distance in the same direction from each other as the elements in the second array. These two arrays can be two separate arrays or part of a larger array. Measurements are taken from the two arrays

and their array correlation matrices are estimated. The eigenvalues and eigenvectors are then computed, and the directionality of the source is determined.

5. Methods of Tracking AOA

When the signal source is mobile (e.g., an UAV), the AOA of the desired signal source changes, and the next task is to track the change in the AOA and steer the beam towards the mobile signal source. Several approaches have been proposed to track the AOA of moving targets using passive arrays [21-24]. Passive arrays do not initiate any signal transmission and are always in the "receiving" mode. A general assumption used in these techniques is that the targets can be approximated as stationary during a limited integration time interval, and the MUSIC algorithm is applied to estimate the AOA parameters at each time interval. Another approach proposed by [21] uses a maximum likelihood algorithm while that proposed by [22] uses a recursive tracking algorithm that uses the AOA estimates from the most recent array data to update the existing one. The approach proposed by [23] attempts to minimize the distance between the components of the true and the estimated array correlation matrices to provide an estimate of the AOA.

In summary, some common AOA estimation and tracking methods were discussed briefly. However, the methods introduced in this section address the signal processing aspects of determining the AOA only and there is also a need to address the question of what type of antenna beam is appropriate for AOA estimation and tracking purposes and whether active or passive detection is suitable. These questions are addressed in the next section.

G. DETECTION AND TRACKING OF UAV

After presenting the methods to estimate and track the AOA of the desired signal sent by the UAV, this section discusses some of the considerations when using arrays for detection and tracking of the UAV.

1. Active and Passive Detection

Figure 20 shows the difference between active and passive detection. For active detection, a sensor cluster constantly searches for the presence of the UAV by sending a predetermined signal and measuring the returned signal characteristics. When the UAV has been detected and its position determined, the sensor cluster initiates beamforming

and tracking of the UAV and performs the task of transmitting the collected data to the UAV through wireless means.

Sensor nodes typically have very limited energy available since they are battery-operated. From an energy dissipation perspective, the passive detection approach is preferred. A passive sensor cluster constantly searches for a predefined signal sent by the UAV. This predefined reference signal may be sent continuously (or at regular time intervals) towards the sensor cluster. The sensor cluster then uses the received signal to determine the AOA of the signal source and initiates beamforming and tracking of the UAV.

The advantage of employing passive detection is that the sensor cluster is not required to transmit signals for detection of the UAV, hence passive detection by the sensor cluster is adopted in this thesis.

UAV

Reflected signal   signal

signal

Sensor cluster

Active Detection   Passive Detection
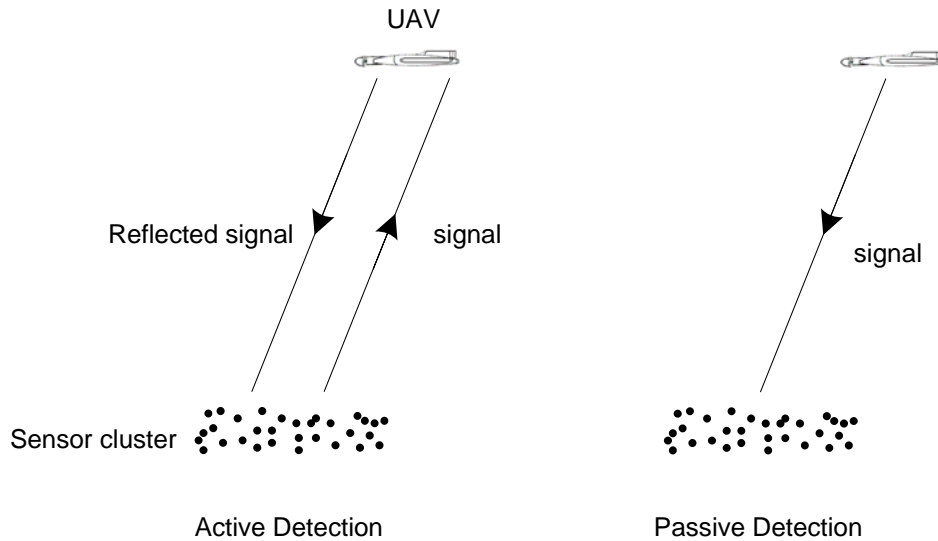
Figure 20.   Active and passive detection of UAV using a sensor cluster.

2.   Detection and Tracking of UAV

A broad beam is especially useful for detection of UAV because of the larger detection region being created as illustrated in Fig. 21. The detection region becomes larger as the altitude increases, making the broad antenna beam a very suitable candidate for UAV detection. Therefore, it is appropriate to use as few array elements as possible to generate a broad beam to detect the UAV in this case.
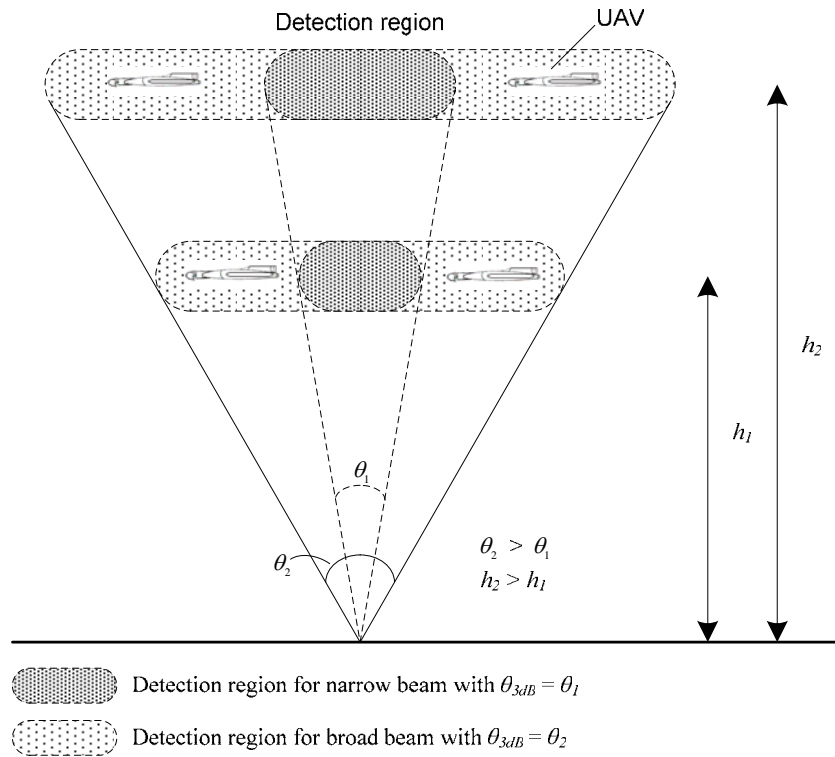
Figure 21.   Generating a broad antenna beam to increase the size of the UAV detection region.

It is often not desirable to use a broad beam to track the UAV because of the lower tracking resolution it provides compared to that of a narrower beam. Figure 22 illustrates how the tracking resolution of a broader beam degrades as the altitude decreases. As shown in the figure, it is not possible to resolve or differentiate between the two UAVs at altitude h_2 because both of their positions reside within the 3-dB beamwdith of the broader beam. Hence, it is more appropriate in this case to use as many array elements as possible in order to generate a narrow beam to provide the tracking resolution required.
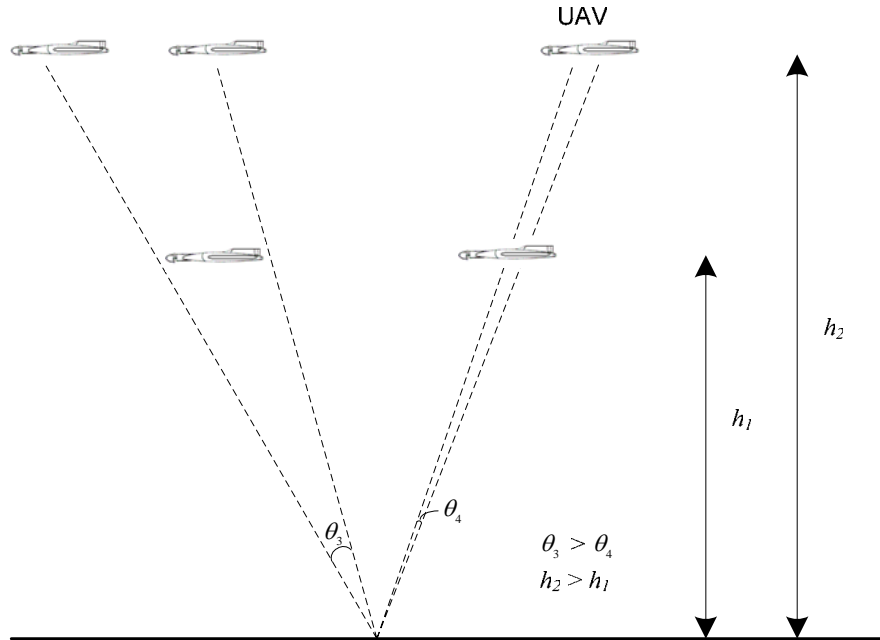
Figure 22.　Generating a narrow beam to increase the tracking resolution of the UAV.

H.　SUMMARY

This chapter presented the fundamental concepts required for each sensor cluster to form an array-like transmission to the UAV. In particular, the array factor and power gain equations of antenna array were presented, followed by a literature review on some findings on random arrays. This was followed by the discussion on the narrowband adaptive beamformer and the various AOA estimation and tracking algorithms using passive arrays. The significance of the antenna beamwidth for UAV detection and tracking was also highlighted.

Up to this point, the relevant discussion has been presented in order to develop a simulation model based on the operation scenario shown in Figures 1 and 2. The simulation model and simulation results are presented in the next chapter. The objective is to study the use of sensor clusters for adaptive beamforming through simulation and compare the simulation results with the theoretical results discussed in Section C of Chapter III.

IV.   SIMULATION RESULTS

A sensor cluster differs from a conventional array in the following aspects: 1) an unknown number of sensor nodes used for beamforming, 2) random positioning of the sensor nodes, 3) position errors due to mobility of sensor nodes and 4) frequent failures of sensor nodes. These are issues found in the design and practical implementation of a wireless sensor network.

This chapter aims to study the effects of the above mentioned issues on the antenna beam used for data transmission from a sensor cluster to an UAV. First, the simulation scenario given in Figures 1 and 2 is presented in greater detail. This is followed by a discussion on the simulation model developed here to study the use of sensor cluster for adaptive beamforming. Next, simulation results are presented and compared to the theoretical findings of random arrays discussed in Section C of Chapter III. The effect of UAV speed on the convergence of the adaptive beamforming algorithm is also discussed.

A.   SIMULATION SCENARIO

This section describes the simulation scenario presented in Figures 1 and 2. The three-dimensional and its equivalent two-dimensional simulation scenario are shown in Figures 23 and 24, respectively. Both figures show the flight path of an UAV which attempts to receive the data collected by the sensor nodes as it flies over them.

The sequence of events for this simulation scenario is described as follows. After the sensor nodes are deployed randomly over an area of interest, they are grouped together into sensor clusters and a primary node is elected for each cluster based on methods described in Section B of Chapter II. It is further assumed that the positions of the secondary nodes within the sensor cluster are determined using methods presented in Section C of Chapter II. Next, an UAV flies over the sensor field and sends a predetermined desired signal to these sensor clusters continuously. Assuming that each sensor cluster has knowledge of the AOA of the desired and interfering signals (based on methods discussed in Chapter III, Section F), it adapts to the change in the AOA of desired

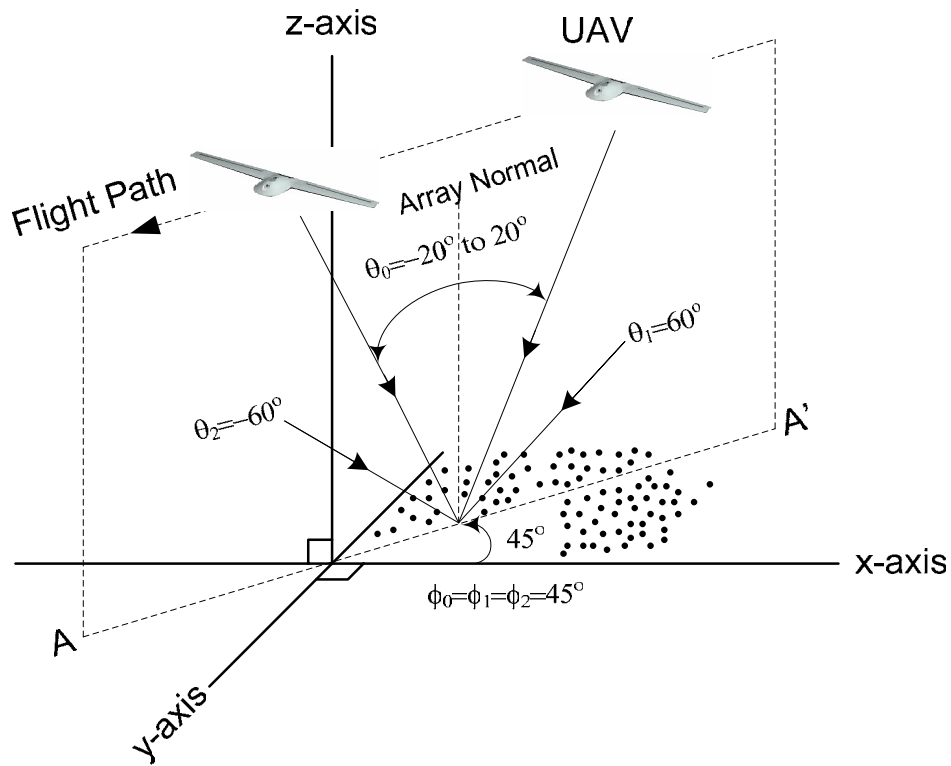Figure 23.   Three-dimensional simulation scenario. The UAV sends a predetermined desired signal towards the sensor clusters in the direction of $\theta_0 = +20°$ to $-20°$ at $\phi_0 = +45°$. The two interference signals arrive at the sensor clusters at $\left(\theta = \pm 60°, \phi = 45°\right)$.
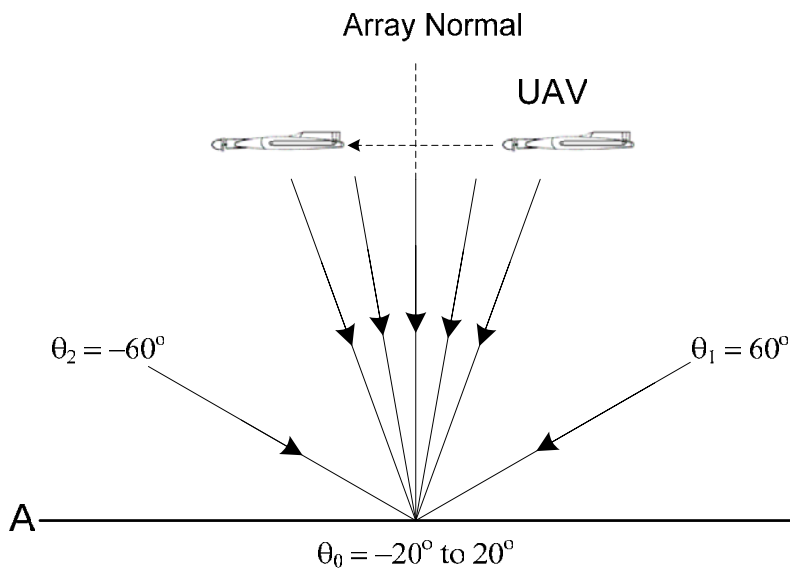

Figure 24.   Two-dimensional diagram showing the scenario in Fig. 23 taken at the plane AA'.

signal sent from the UAV and steers the antenna beam towards the UAV using the LMS algorithm. The following assumptions apply to this simulation scenario:

1. Passive detection of the UAV by the sensor cluster array as discussed in Chapter III, Section G.1.

2. The desired complex modulating signal *s(t)* sent by the UAV is known to the sensor cluster array and is the same as the reference signal *r(t)* used for the LMS algorithm.

3. Each primary node has perfect knowledge of its own position and the position of the secondary nodes within the sensor cluster prior to beamforming.

4. The AOA of the desired signal (θ_0, ϕ_0) is known to the sensor cluster. The elevation angle θ_0 spans from $+20°$ to $-20°$ and the azimuth angle ϕ_0 is fixed at $+45°$.

5. The AOA of the first interference signal (θ_1, ϕ_1) is known to the sensor cluster and is fixed at elevation angle $\theta_1 = +60°$ and azimuth angle $\phi_1 = +45°$.

6. The AOA of the second interference signal (θ_2, ϕ_2) is known to the sensor cluster and is fixed at elevation angle $\theta_2 = -60°$ and azimuth angle $\phi_2 = +45°$.

7. There is perfect frequency, phase and data synchronization among all the sensor nodes within the sensor cluster and between the UAV and each sensor cluster.

8. There is perfect coordination among the primary node and the secondary nodes within a sensor cluster for beamforming.

9. All sensor cluster arrays are designated to operate at a carrier frequency of 500 MHz (i.e., $\lambda = 0.6$ m).

10. All sensor nodes are modeled as isotropic antenna elements and mutual-coupling between sensor nodes is not considered.

The description of the simulation scenario and its assumptions set the baseline for the development of the simulation model presented in the next section.

B.   SIMULATION MODEL

Figure 25 shows the simulation model used in this thesis. The model was implemented in MATLAB programming language and the program descriptions are found in the Appendix.
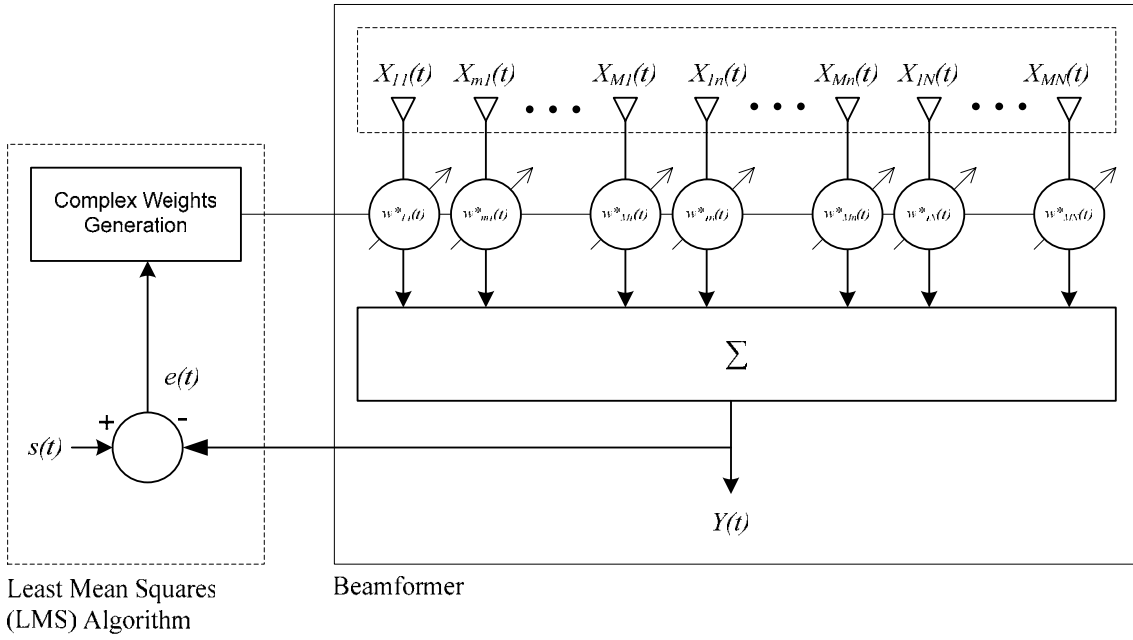

Figure 25.   Simulation model for $M \times N$ adaptive narrow-band beamformer. The complex weights are adjusted by the LMS algorithm and its outputs are applied to the array elements to form a beam.

As mentioned in the previous section, the desired complex modulating signal $s(t)$ sent by the UAV is known to the sensor cluster array and becomes the reference signal for the LMS algorithm. The array signal generator generates the array outputs $\underline{X}'(t)$ given by

$$\underline{X}'(t) = s(t)\underline{v}' + \underline{n}'(t) + z_1(t)\underline{u}'_1 + z_2(t)\underline{u}'_2 \tag{46}$$

which is a modified version of Equation (33). For convenience, the desired complex modulating signal $s(t)$ is assumed to be a real-valued modulating signal given by

46

$$s(t) = \sin\left(\frac{2\pi ft}{f_s} + \psi_0\right) \quad (47)$$

where f is the frequency in Hz, t is the discrete time in seconds, f_s is the number of samples per second (or sampling rate) and ψ_0 is a uniform random variable in the range 0 to 2π. The steering vector $\underset{\sim}{v}'$ associated with the direction (θ_0, ϕ_0) of the desired signal is a two dimensional $M{\times}N$ vector given by

$$\underset{\sim}{v}' = \begin{bmatrix} e^{j\omega t_{11}(\theta_0,\phi_0)} & \cdots & e^{j\omega t_{m1}(\theta_0,\phi_0)} & \cdots & e^{j\omega t_{M1}(\theta_0,\phi_0)} \\ \vdots & & \vdots & & \vdots \\ e^{j\omega t_{1n}(\theta_0,\phi_0)} & \cdots & e^{j\omega t_{mn}(\theta_0,\phi_0)} & \cdots & e^{j\omega t_{Mn}(\theta_0,\phi_0)} \\ \vdots & & \vdots & & \vdots \\ e^{j\omega t_{1N}(\theta_0,\phi_0)} & \cdots & e^{j\omega t_{mN}(\theta_0,\phi_0)} & \cdots & e^{j\omega t_{MN}(\theta_0,\phi_0)} \end{bmatrix} \quad (48)$$

which is a modified version of Equation (34) in which $\underset{\sim}{v}$ was an $MN{\times}1$ vector. The one-dimensional representation is a more convenient form of mathematical representation while the two-dimensional representation is preferred for MATLAB implementation and is adopted in this chapter. Similarly, $\underset{\sim}{n}'(t)$ is an $M{\times}N$ noise matrix given by

$$\underset{\sim}{n}'(t) = \begin{bmatrix} n_{11}(t) & \cdots & n_{m1}(t) & \cdots & n_{M1}(t) \\ \vdots & & \vdots & & \vdots \\ n_{1n}(t) & \cdots & n_{mn}(t) & \cdots & n_{Mn}(t) \\ \vdots & & \vdots & & \vdots \\ n_{1N}(t) & \cdots & n_{mN}(t) & \cdots & n_{MN}(t) \end{bmatrix} \quad (49)$$

which is a modified version of Equation (35).

The two interfering modulating signals $z_1(t)$ and $z_2(t)$ with the corresponding steering vectors $\underset{\sim}{u}'_1$ and $\underset{\sim}{u}'_2$, respectively, are also included in Equation (46). The objective is to steer the main beam in the direction of the desired signal and suppress the interference signals by creating nulls in their directions. The first interfering modulating signal $z_1(t)$ is given by

$$z_1(t) = \sin\left(\frac{2\pi ft}{f_s} + \psi_1\right)$$ (50)

where ψ_1 is an uniform random variable in the range 0 to 2π. The steering vector $\underline{u}_1'$ associated with the direction (θ_1, ϕ_1) of the first interference signal is an $M{\times}N$ matrix given by

$$\underline{u}_1' = \begin{bmatrix} e^{j\omega t_{11}(\theta_1,\phi_1)} & \cdots & e^{j\omega t_{m1}(\theta_1,\phi_1)} & \cdots & e^{j\omega t_{M1}(\theta_1,\phi_1)} \\ \vdots & & \vdots & & \vdots \\ e^{j\omega t_{1n}(\theta_1,\phi_1)} & \cdots & e^{j\omega t_{mn}(\theta_1,\phi_1)} & \cdots & e^{j\omega t_{Mn}(\theta_1,\phi_1)} \\ \vdots & & \vdots & & \vdots \\ e^{j\omega t_{1N}(\theta_1,\phi_1)} & \cdots & e^{j\omega t_{mN}(\theta_1,\phi_1)} & \cdots & e^{j\omega t_{MN}(\theta_1,\phi_1)} \end{bmatrix}.$$ (51)

The second interfering modulating signal $z_2(t)$ is given by

$$z_2(t) = \sin\left(\frac{2\pi ft}{f_s} + \psi_2\right)$$ (52)

where ψ_2 is a uniform random variable in the range 0 to 2π. The steering vector $\underline{u}_2'$ associated with the direction (θ_2, ϕ_2) of the second interference signal is an $M{\times}N$ matrix given by

$$\underline{u}_2' = \begin{bmatrix} e^{j\omega t_{11}(\theta_2,\phi_2)} & \cdots & e^{j\omega t_{m1}(\theta_2,\phi_2)} & \cdots & e^{j\omega t_{M1}(\theta_2,\phi_2)} \\ \vdots & & \vdots & & \vdots \\ e^{j\omega t_{1n}(\theta_2,\phi_2)} & \cdots & e^{j\omega t_{mn}(\theta_2,\phi_2)} & \cdots & e^{j\omega t_{Mn}(\theta_2,\phi_2)} \\ \vdots & & \vdots & & \vdots \\ e^{j\omega t_{1N}(\theta_2,\phi_2)} & \cdots & e^{j\omega t_{mN}(\theta_2,\phi_2)} & \cdots & e^{j\omega t_{MN}(\theta_2,\phi_2)} \end{bmatrix}.$$ (53)

The array output $\underline{X}'(t)$ is an $M{\times}N$ matrix given by

$$\underline{X}'(t) = \begin{bmatrix} X_{11}(t) & \cdots & X_{m1}(t) & \cdots & X_{M1}(t) \\ \vdots & & \vdots & & \vdots \\ X_{1n}(t) & \cdots & X_{mn}(t) & \cdots & X_{Mn}(t) \\ \vdots & & \vdots & & \vdots \\ X_{1N}(t) & \cdots & X_{mN}(t) & \cdots & X_{MN}(t) \end{bmatrix}$$ (54)

which is a modified version of Equation (38).

The output vector of the beamformer $\underset{\sim}{Y}'(t)$ is given by

$$\underset{\sim}{Y}'(t) = \underset{\sim}{w}'^{*}(t) \bullet \underset{\sim}{X}'(t) \tag{55}$$

where $\bullet$ denotes dot product and $\underset{\sim}{w}'^{*}(t)$ is an $M{\times}N$ weight matrix given by

$$\underset{\sim}{w}'^{*}(t) = \begin{bmatrix} w_{11}^{*}(t) & \cdots & w_{m1}^{*}(t) & \cdots & w_{M1}^{*}(t) \\ \vdots & & \vdots & & \vdots \\ w_{1n}^{*}(t) & \cdots & w_{mn}^{*}(t) & \cdots & w_{Mn}^{*}(t) \\ \vdots & & \vdots & & \vdots \\ w_{1N}^{*}(t) & \cdots & w_{mN}^{*}(t) & \cdots & w_{MN}^{*}(t) \end{bmatrix} \tag{56}$$

which is a modified version of Equation (37). Therefore, $\underset{\sim}{Y}'(t)$ becomes an an $M{\times}N$ matrix given by

$$\underset{\sim}{Y}'(t) = \begin{bmatrix} Y_{11}(t) & \cdots & Y_{m1}(t) & \cdots & Y_{M1}(t) \\ \vdots & & \vdots & & \vdots \\ Y_{1n}(t) & \cdots & Y_{mn}(t) & \cdots & Y_{Mn}(t) \\ \vdots & & \vdots & & \vdots \\ Y_{1N}(t) & \cdots & Y_{mN}(t) & \cdots & Y_{MN}(t) \end{bmatrix} \tag{57}$$

The beamformer output $Y(t)$ given in Equation (36) is obtained by summing all the matrix elements within the $\underset{\sim}{Y}'(t)$ matrix given in Equation (57).

The simulation procedure is to sample $s(t)$, $z_1(t)$ and $z_2(t)$ at f_s, and the complex weights are computed for each iteration t using the LMS algorithm. The algorithm is said to have converged when $E\left[e^2(t)\right] \leq 0.1$, which is defined as the convergence threshold. The complex weights generated are then used to compute the array factor using Equation (23) and plot the beam pattern (or power gain) using Equation (24).

C.   EFFECTS OF SENSOR NODE DENSITY

In this section, the effects of the number of sensor nodes on the antenna beam generated by a sensor cluster are presented. The location of each node is assumed to be uniformly distributed within a $1.2{\times}1.2$ m^2 plane; hence, changing the number of sensor nodes within the sensor cluster is equivalent to changing the density of sensor nodes within the cluster. The simulation was performed by assuming that the AOA of the de-

sired signal is at $\theta_0 = 0°$ and $\phi_0 = +45°$. One hundred sets of sensor clusters are generated for each sensor node density and the corresponding power gains computed. The average power gain is then obtained by averaging these results. This method of obtaining the average power gain is adopted throughout the chapter.

The interference rejection level I_R indicates how well the antenna beam can suppress the interference level. A high I_R level is desirable in the direction of the interference signal. Figure 26 shows the plots of the antenna beam pattern for sensor cluster densities ranging from 3×3 to 16×16 sensor nodes. It can be seen that the 3-dB beamwidth and the shape of the main lobe remain relatively unchanged as the number of sensor nodes change. However, the maximum average power gain $\overline{G}_{max}$ and the interference rejection level I_R decreases as the number of sensor nodes is decreased to less than 7×7. Figure 27 shows that $\overline{G}_{max}$ has reduced from 0 dB for the 7×7 sensor cluster to -3.3 dB for the 3×3 sensor cluster while Fig. 28 shows that the interference rejection is reduced from 55 dB for the 9×9 sensor cluster to 17 dB for the 3×3 sensor cluster.

These results are consistent with those discussed in Chapter III, Section C.1 where the results derived by [7] suggested that the average sidelobe level can be reduced by increasing the density of the sensor nodes within the cluster. In our case here, increasing the number of sensor nodes enabled the reduction of the average sidelobe levels and hence suppressed the interference signals more effectively.
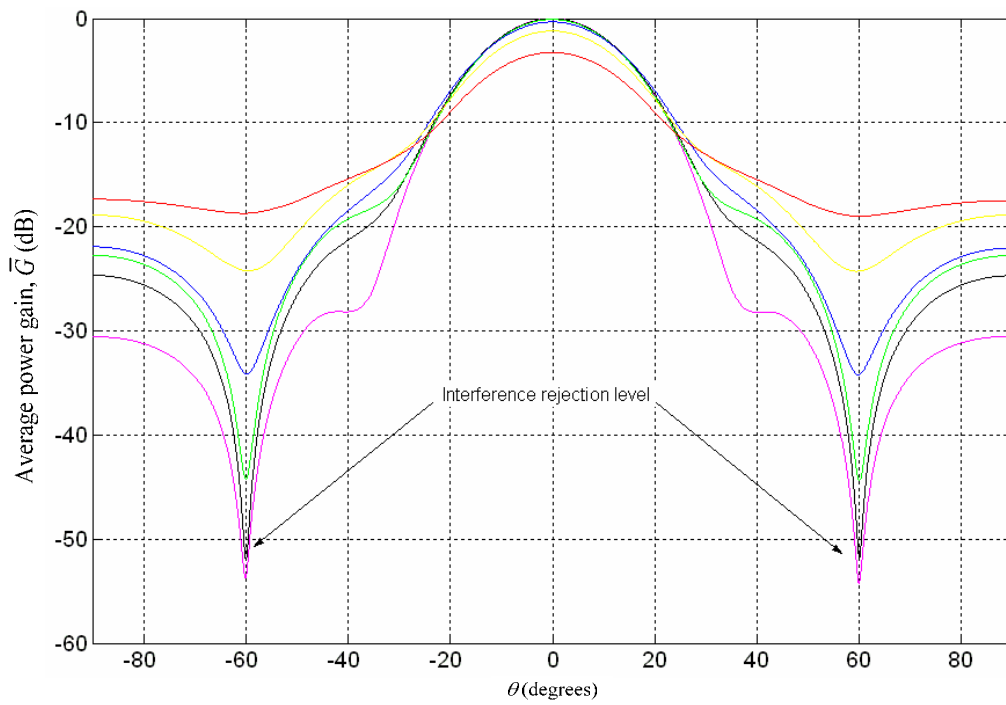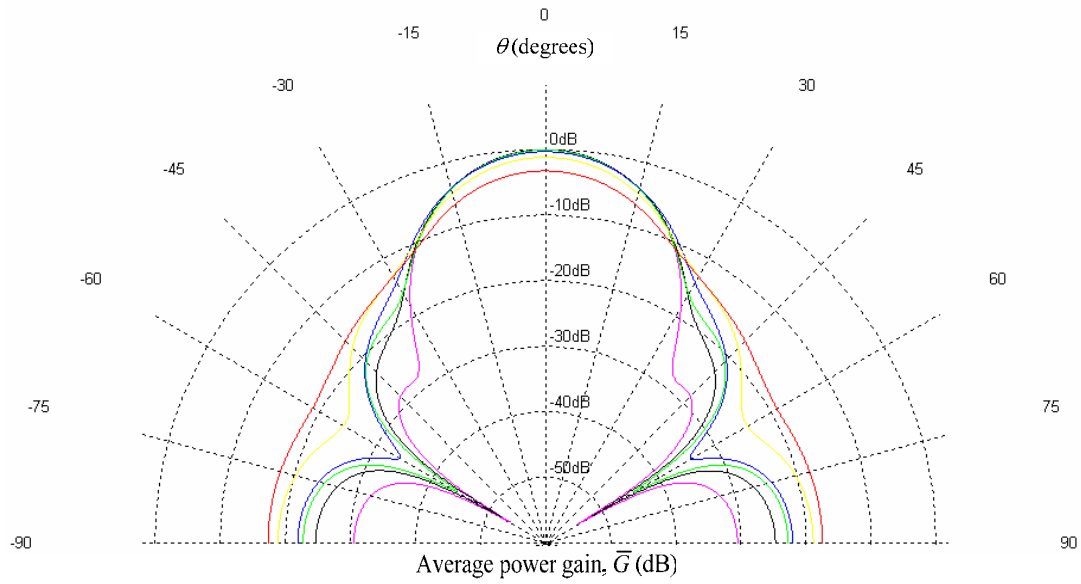
Figure 26.   Average power gain of the beams generated by 16×16, 7×7, 6×6, 5×5, 4×4 and 3×3 sensor clusters at $\left(\theta_0,\phi_0\right)=\left(0°,45°\right)$: (a) Polar plots and (b) X-Y plots showing the decrease in maximum average power gain and interference rejection level as the number of sensor nodes decreased.
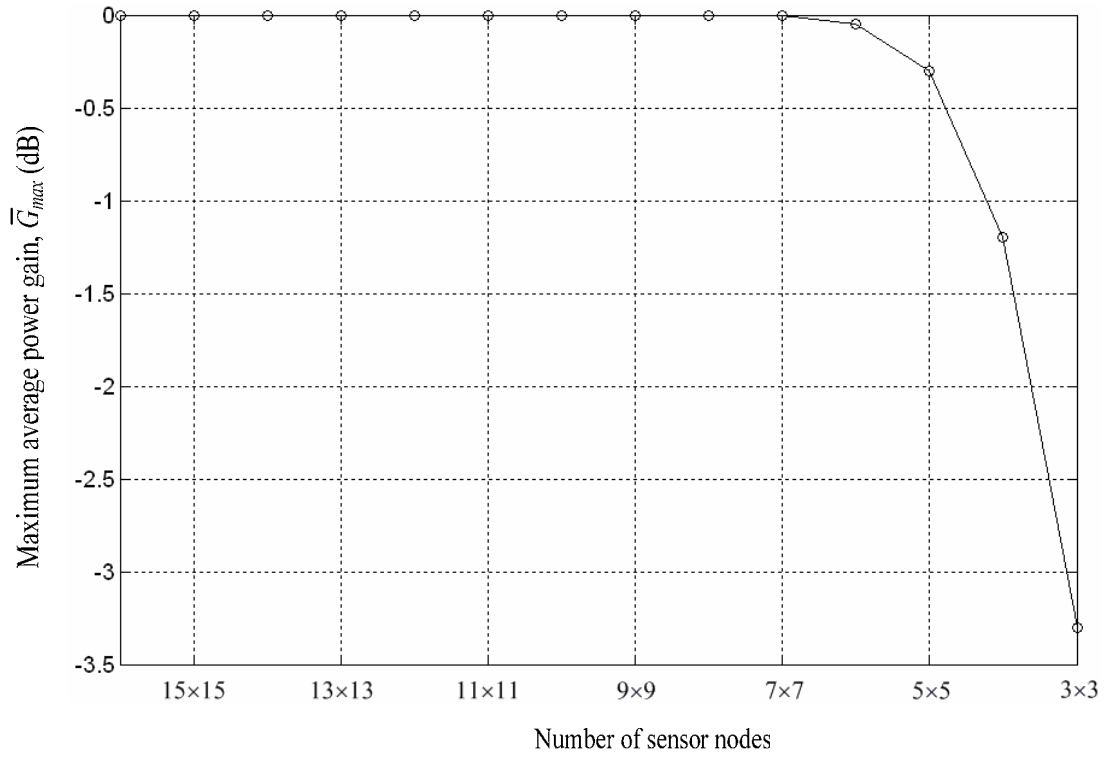
51

Figure 27.   The maximum average power gain as a function of the number of sensor nodes.
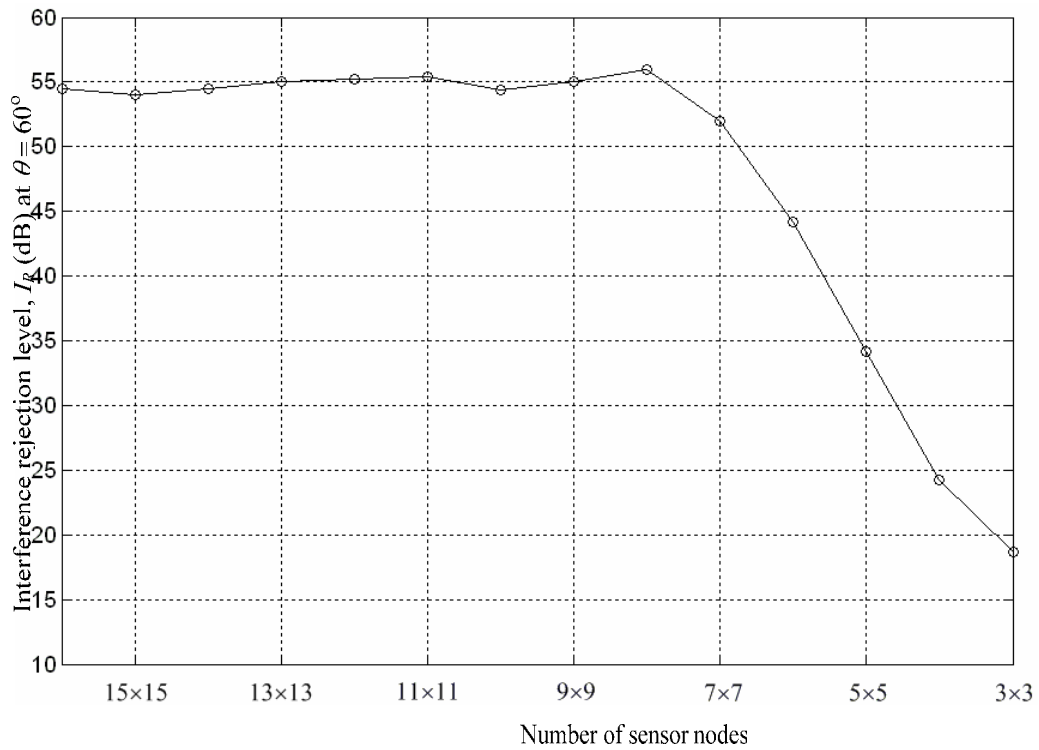

Figure 28.   The interference rejection level as a function of the number of sensor nodes.

D. EFFECTS OF POSITION ERRORS

It was assumed that the primary node has perfect information of the initial locations of the secondary nodes (using the location discovery methods described in Chapter II) prior to beamforming. In reality, there may be errors associated with these location discovery methods. Moreover, the positions of these mobile sensor nodes may change without the knowledge of the primary node during the beamforming process. These cause position errors (or phase errors). The consequence is that the complex weights used for beamforming are being adjusted without accounting for the change in the locations of the sensor nodes. This affects the average antenna array factor and, hence, the average beam pattern (or average power gain).

In this section, the effects of position errors on the antenna beam generated by a 7×7 sensor cluster are presented. It is assumed that the sensor nodes move much slower than the speed of the UAV and move within a distance of $\pm\Delta d$ from their initial locations known to the primary node. Therefore, Δd is regarded as the position error. In particular, five values of Δd are considered: 0.1λ, 0.2λ, 0.3λ, 0.4λ, and 0.5λ, where $\lambda = 0.6$ m. The simulation was performed by assuming that the AOA of the desired signal is at $\theta_0 = 0°$ and $\phi_0 = +45°$.

Figure 29 shows the plots of the antenna beam pattern for different values of Δd. It shows that the maximum average power gain and the 3-dB beamwidth are not affected significantly by the magnitude of Δd. This result is better than that discussed in Chapter III, Section 2, where it was shown that a phase error of $\pm40°$ is required to cause a 3-dB reduction in the maximum average power gain. In this case, the maximum average power gain remained the same even though the phase error was 0.5λ (or $\pm90°$).

It can be seen from Fig. 29 that the interference rejection level I_R decreased when Δd increased. Figure 30 shows that the value of I_R decreased from 28 dB when $\Delta d = 0.1\lambda$ to 23 dB when $\Delta d = 0.2\lambda$, a reduction of 5 dB when Δd is doubled. Similarly, the value of I_R reduced by 5 dB from 23 dB to 17 dB when Δd increased from 0.2λ to 0.4λ. This is 1 dB less than that discussed in Chapter III, Section 2.

(a)

(b)

—— No position errors	—— $\Delta d = 0.3\lambda$ (18 cm)	2-D plots generated at $\phi = 45°$
—— $\Delta d = 0.1\lambda$ (6 cm)	—— $\Delta d = 0.4\lambda$ (24 cm)	
—— $\Delta d = 0.2\lambda$ (12 cm)	—— $\Delta d = 0.5\lambda$ (30 cm)	

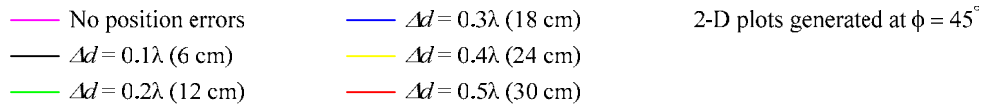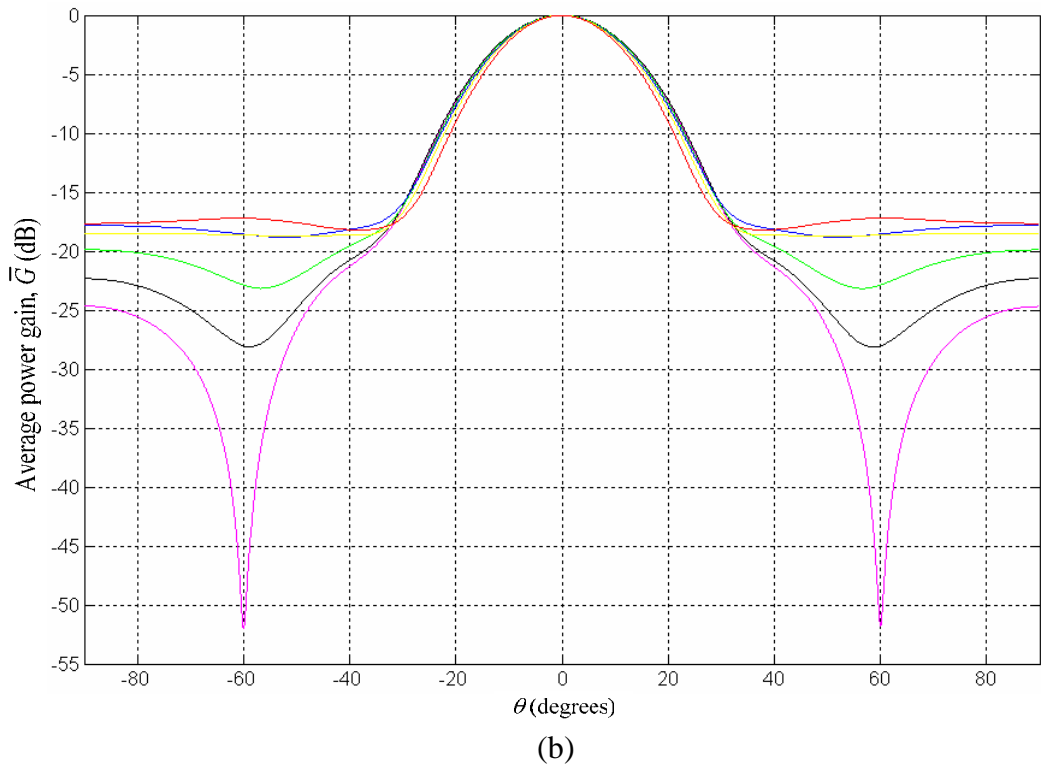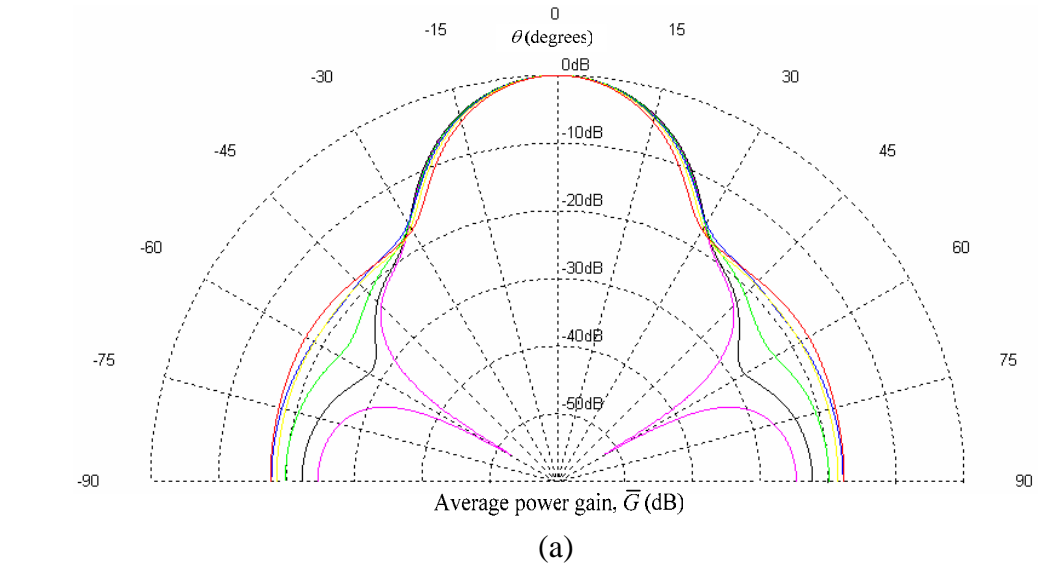Figure 29.   Average power gain of the beams generated by the 7×7 sensor cluster in the presence of position errors $\Delta d = 0.1\lambda$, 0.2λ, 0.3λ, 0.4λ, and 0.5λ at $(\theta_0, \phi_0) = (0°, 45°)$: (a) Polar plots and (b) X-Y plots showing the decrease in interference rejection level as the position errors increased.
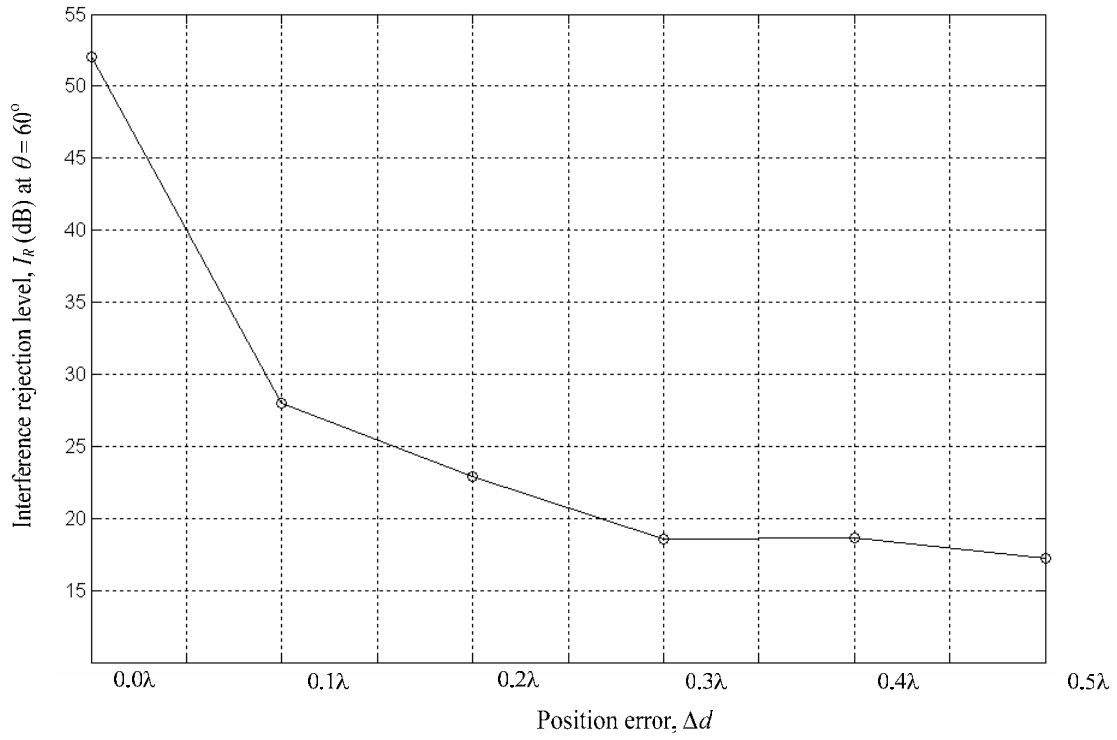
Figure 30.   The interference rejection level as a function of position error.

E.   EFFECTS OF SENSOR NODE FAILURES

Sensor nodes fail frequently in wireless sensor networks due to depleted battery energy or damaged by environmental conditions. The effects of sensor node failures on the antenna beam being generated by the sensor cluster are presented in this section using a 7×7 sensor cluster.

The simulation was performed by assuming that the AOA of the desired signal is at $\theta_0 = 0°$ and $\phi_0 = +45°$. Figure 31 shows the antenna beam pattern produced by the 7×7 sensor cluster for five cases: 1) no element fails, 2) five elements fail, 3) ten elements fail, 4) fifteen elements fail and 5) twenty elements fail. It shows that the 3-dB beam-width and the shape of the main lobe remain relatively unchanged in the presence of sensor node failures. However, there is some reduction in the maximum average power gain as the number of sensor node failures increases. For example, the maximum average power gain is reduced by 4.65 dB when twenty sensor nodes failed compared to the case when no sensor nodes failed. This is expected since the magnitude (of the complex weights) contribution from the sensor nodes decreases due to sensor node failures. Additionally, the interference rejection levels decreased as the number of sensor node failures increased, thus reducing the sensor cluster's capability to create nulls at the AOA of the two interfering signals at $\theta = \pm 60°$. The interference rejection level was about 52 dB when no sensor nodes failed and reduced to about 23.75 dB when twenty sensor nodes failed. Hence, sensor node failures do not affect the 3-dB beamwidth and the shape of the main lobe significantly, but the maximum average power gain and the interference rejection levels of the antenna beam generated by the sensor cluster are reduced considerably.

Figure 32 shows the reduction in maximum average power gain $\overline{G}_{max}$ as the number of sensor node failures increases. The simulated results showed good agreement with that calculated using Equation (28). It has reduced from 0 dB in the absence of sensor node failures to about 4.6 dB when twenty sensor nodes failed. Figure 33 shows that the interference rejection has reduced from 50 dB in the absence of sensor node failures to about 24 dB when twenty sensor nodes failed.

(a)

(b)
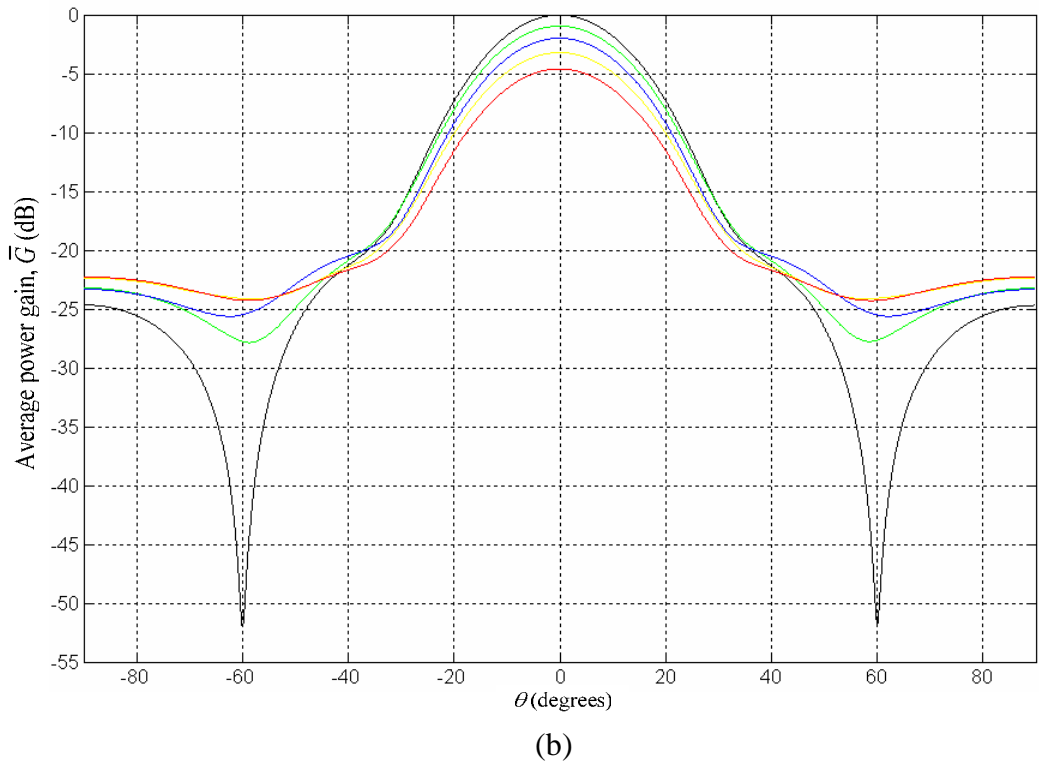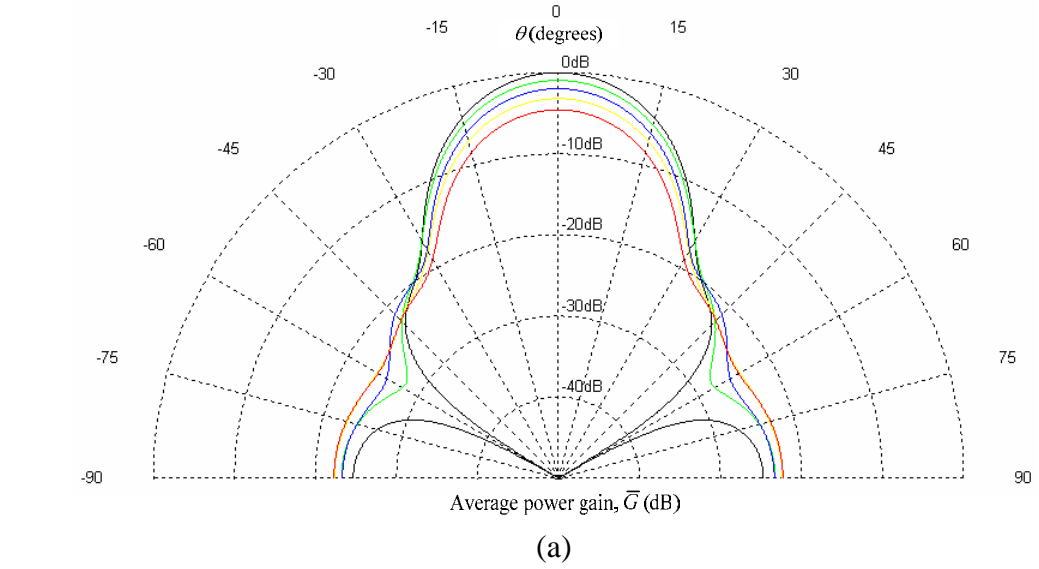
No sensor nodes failed   15 sensor nodes failed   2-D plots generated at $\phi = 45^{\circ}$

5 sensor nodes failed   20 sensor nodes failed

10 sensor nodes failed

Figure 31.　Average power gain of the beams generated by the 7×7 sensor cluster as the number of sensor node failures increased from five to twenty at $\left(\theta_0, \phi_0\right) = \left(0^{\circ}, 45^{\circ}\right)$: (a) Polar plots and (b) X-Y plots showing the decrease in maximum average power gain and interference rejection level as the number of sensor node failures increased.
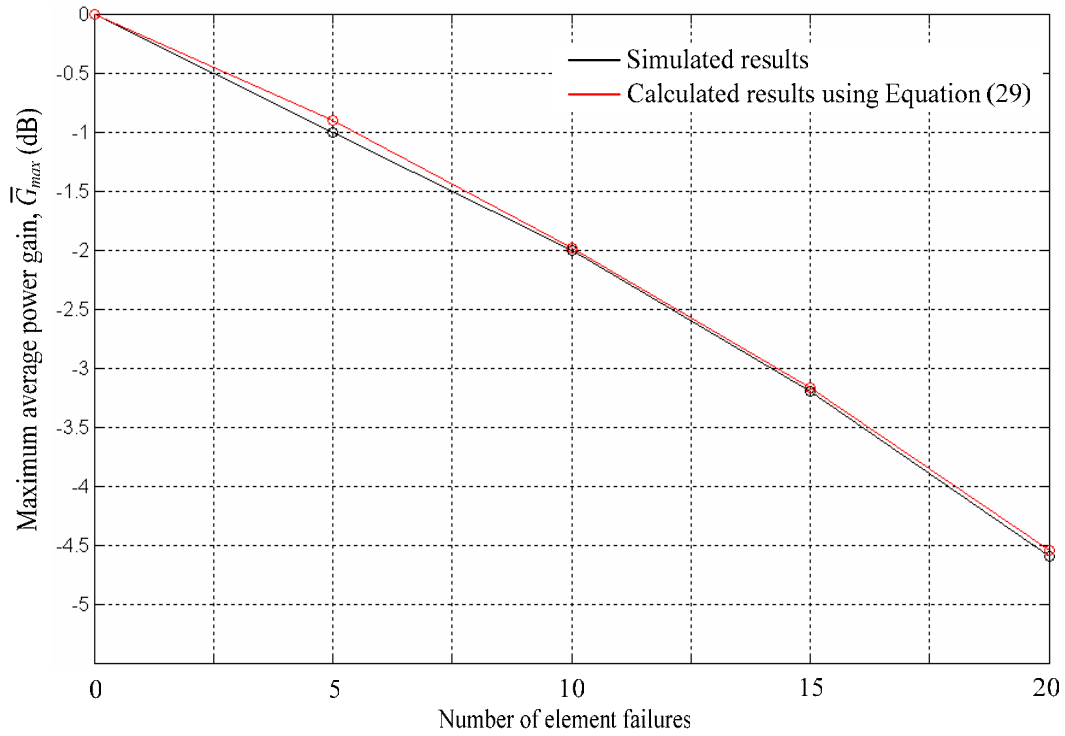
57

Figure 32.   The maximum average power gain as a function of sensor node failures.
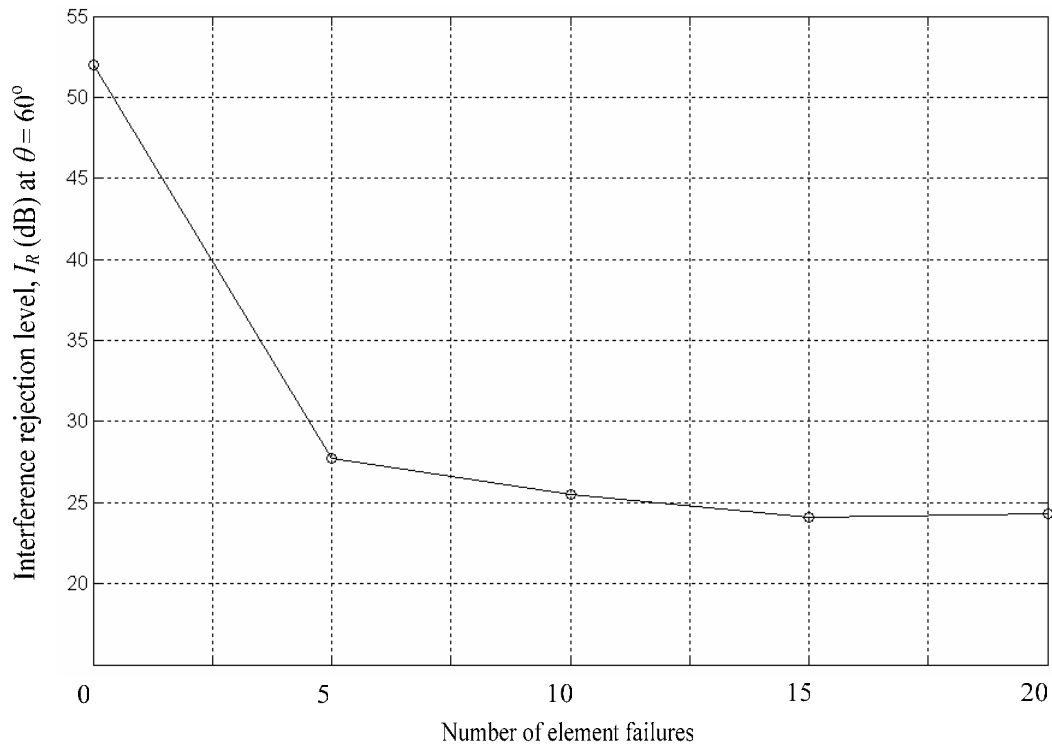

Figure 33.   The interference rejection level as a function of sensor node failures.

F. ADAPTIVE BEAMFORMING USING SENSOR CLUSTERS

Adaptive beamforming is implemented in simulation to steer the antenna beam towards the UAV as it flies from $\theta_0 = +20°$ to $-20°$ at $\phi_0 = +45°$ using the LMS algorithm. This section contains a series of plots illustrating the effects of position errors and sensor node failures on the antenna beam pattern (or average power gain) generated by the 7×7 sensor cluster. In particular, five cases are presented:

1. AOA of the desired signal at $(\theta_0, \phi_0) = (20°, 45°)$. No position errors and sensor node failures are experienced within the sensor cluster.

2. AOA of the desired signal at $(\theta_0, \phi_0) = (10°, 45°)$. Position errors of $\Delta d = 0.1\lambda$ and five sensor node failures are simulated within the sensor cluster.

3. AOA of the desired signal at $(\theta_0, \phi_0) = (0°, 45°)$. Position errors of $\Delta d = 0.2\lambda$ and ten sensor node failures are simulated within the sensor cluster.

4. AOA of the desired signal at $(\theta_0, \phi_0) = (-10°, 45°)$. Position errors of $\Delta d = 0.3\lambda$ and fifteen sensor node failures are simulated within the sensor cluster.

5. AOA of the desired signal at $(\theta_0, \phi_0) = (-20°, 45°)$. Position errors of $\Delta d = 0.4\lambda$ and twenty sensor node failures are simulated within the sensor cluster.

For each case, the antenna beam generated by the sensor cluster in the presence of position errors and sensor node failures are shown.

Figure 34 shows the two-dimensional plots of the antenna average power gain versus the elevation angle θ for case 1. It can be seen that the maximum average power gain occurs at $\theta = 20°$, and nulls are created at $\theta = \pm60°$. This shows that the sensor cluster can steer the main lobe towards the AOA of the desired signal and suppress the interference signals simultaneously. The highest sidelobe level is about 20 dB below the main lobe, and the interference rejection level is about 52 dB.

Figure 35 shows the two-dimensional plots of the antenna average power gain versus the elevation angle θ for case 2. It can be seen that the sensor cluster managed to steer the beam towards the AOA of the desired signal. The shape of the main lobe and the 3-dB beamwidth also remain relatively unchanged under these conditions. However, the maximum average power gain has reduced by 1 dB while the interference rejection ratio has reduced to about 25 dB at $\theta = -60°$ and 26 dB at $\theta = 60°$.

Figure 36 shows the two-dimensional plots of the antenna average power gain versus the elevation angle θ for case 3. It can be seen that the sensor cluster still managed to steer the beam towards the AOA of the desired signal. The shape of the main lobe and the 3-dB beamwidth also remain relatively unchanged under these conditions. However, the maximum average power gain has reduced by 2 dB while the interference rejection ratio has reduced to about 22 dB at $\theta = \pm60°$.

Figure 37 shows the two-dimensional plots of the antenna average power gain versus the elevation angle θ for case 4. It can be seen that the main lobe points towards the AOA of the desired signal and the shape of the main lobe and the 3-dB beamwidth also remain relatively unchanged under these conditions. However, the maximum average power gain is reduced by 3.3 dB while the interference rejection ratio is reduced to about 21 dB at $\theta = -60°$ and 22 dB at $\theta = 60°$.

Figure 38 shows the two-dimensional plots of the antenna average power gain versus the elevation angle θ for case 5. It can be seen that the main lobe points at $\theta = -15°$ instead of $-20°$, a main lobe pointing error of $5°$. This shows that the sensor cluster is unable to steer the beam towards the AOA of the desired signal when $\Delta d = 0.4\lambda$ wavelength and 20 sensor nodes failed. The maximum average power gain has reduced by 5.5 dB while the interference rejection ratio has reduced to about 20 dB at $\theta = -60°$, and 20.5 dB at $\theta = 60°$.

Figure 39 shows the reduction in maximum average power gain $\overline{G}_{max}$ as the position errors and sensor node failures increase. It has reduced from 0 dB in case 1 to about 5.5 dB in case 5. Figure 40 shows that the interference rejection has reduced from 50 dB in case 1 to 13 dB in case 5. Both figures show that as the sensor cluster beamforms to-

wards the UAV, the maximum average power gain and the interference rejection levels of the antenna beam decrease when the position errors and sensor node failures increase.
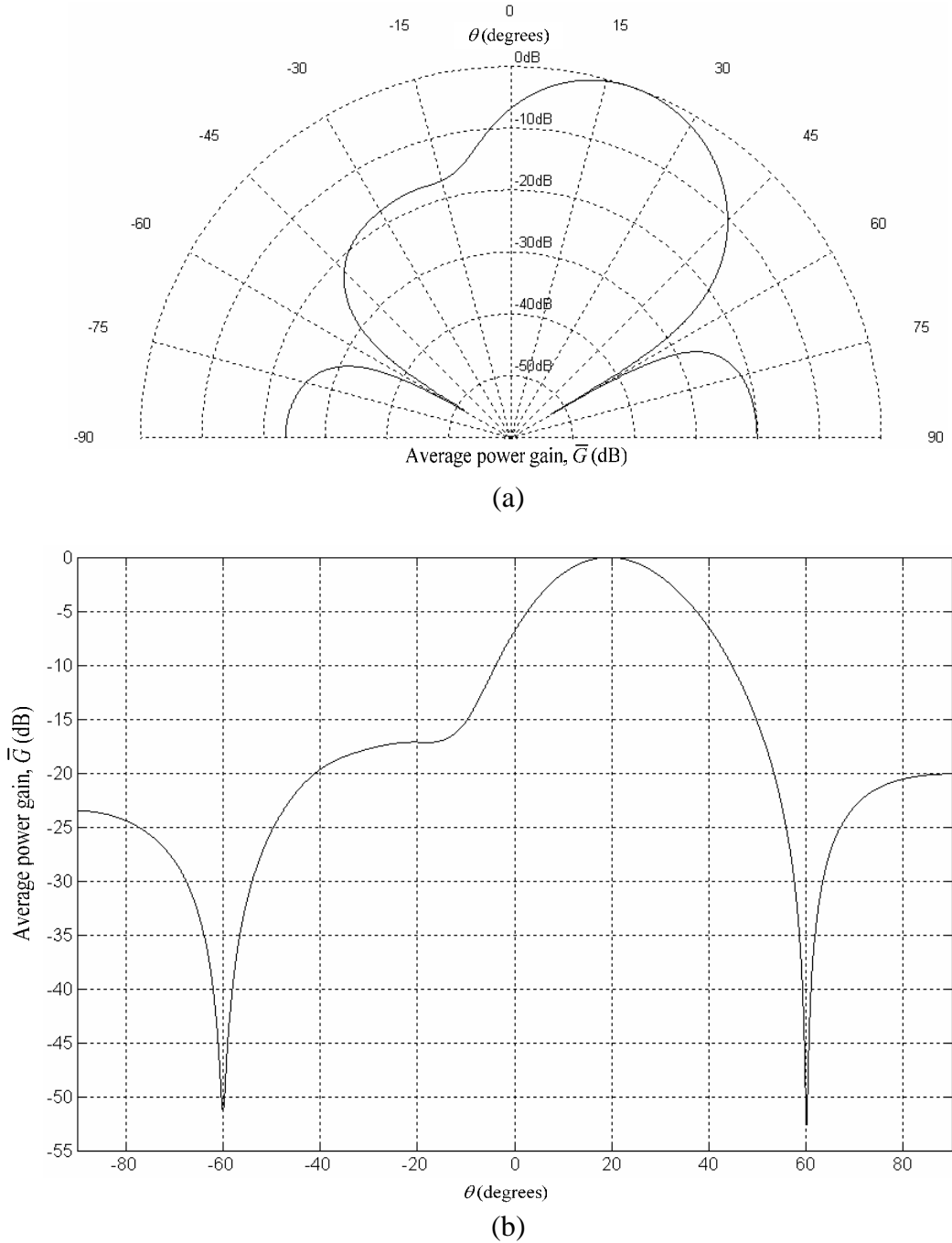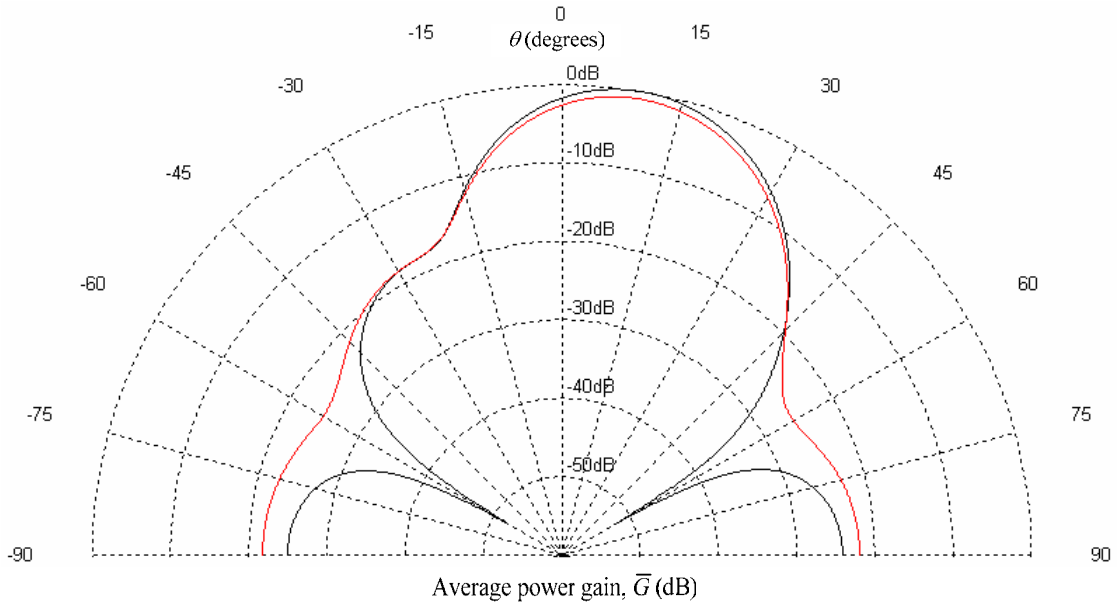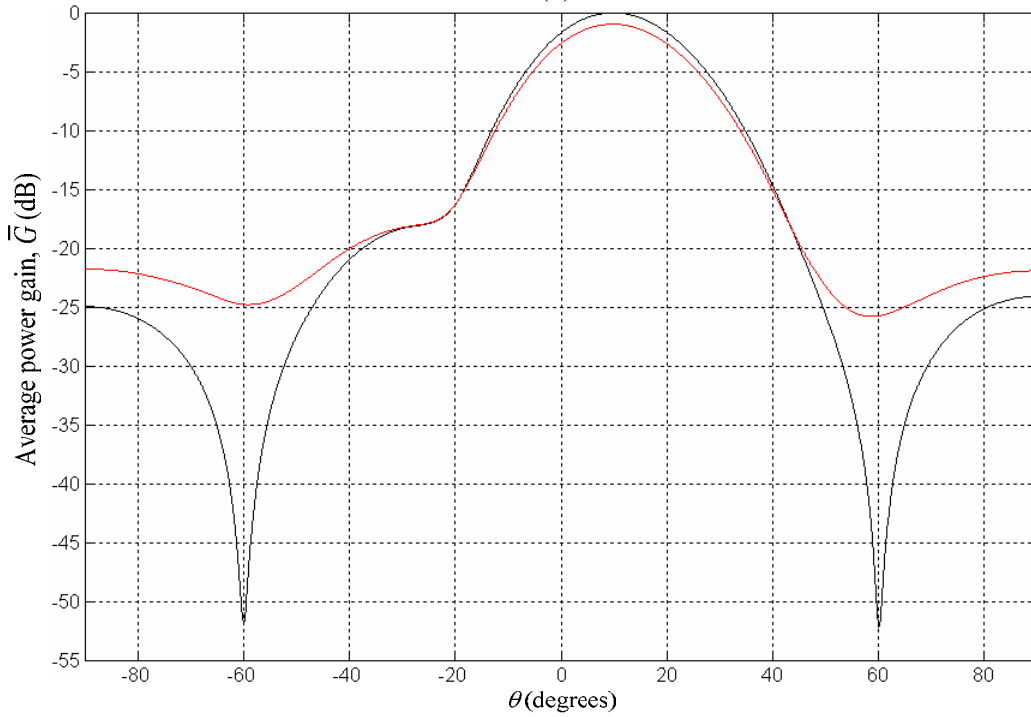

(a)

(b)

Figure 34.   Average power gain of the beams generated by the 7×7 sensor cluster in the absence of position errors and sensor node failures at $\left(\theta_0,\phi_0\right)=\left(20^\circ,45^\circ\right)$: (a) Polar plot and (b) X-Y plot showing the maximum average power gain of 0 dB and interference rejection level of 52 dB and 55 dB at $\theta=60^\circ$ and $\theta=-60^\circ$, respectively.

Figure 35. Average power gain of the beams generated by the 7×7 sensor cluster in the presence of position errors $\Delta d = 0.1\lambda$ and five sensor node failures at $(\theta_0, \phi_0) = (10°, 45°)$: (a) Polar plots and (b) X-Y plots showing the decrease in maximum average power gain and interference rejection level.
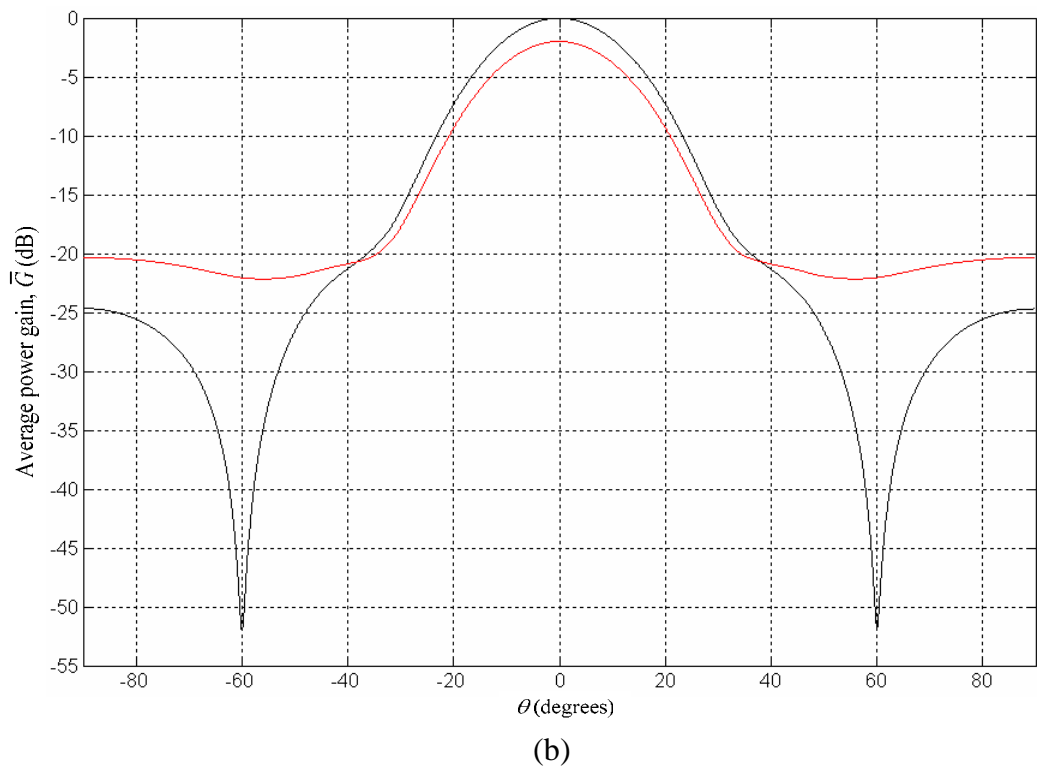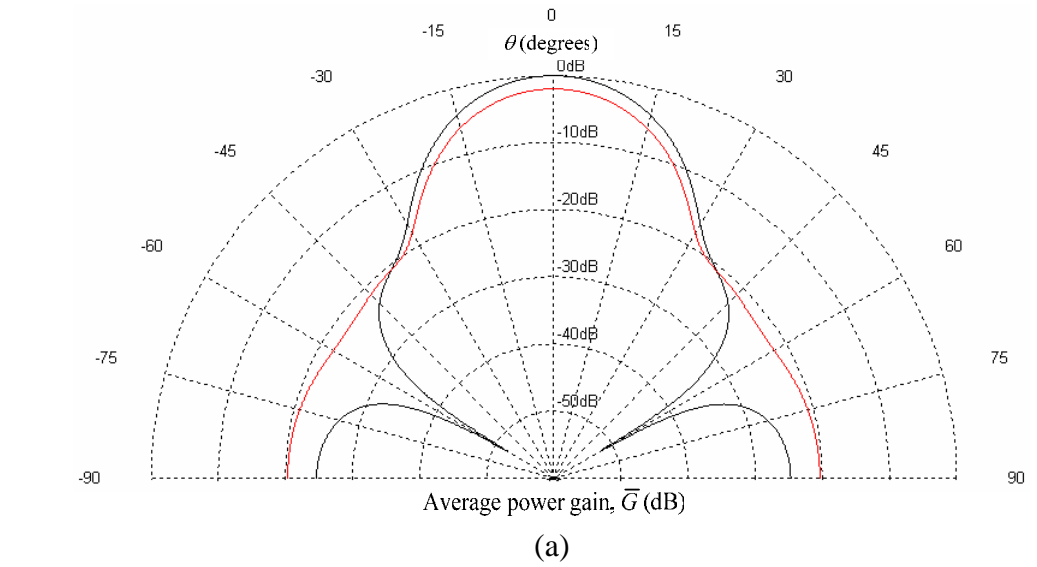
(a)

(b)

Absence of position errors and sensor node failures

Presence of position errors ($\Delta d = 0.2\lambda$) and 10 sensor node failures

2-D plots generated at $\phi = 45^\circ$

Figure 36.   Average power gain of the beams generated by the 7×7 sensor cluster in the pres-
ence of position errors $\Delta d = 0.2\lambda$ and ten sensor node failures at $(\theta_0, \phi_0) = (0^\circ, 45^\circ)$: (a)
Polar plots and (b) X-Y plots showing further decrease in maximum average power gain
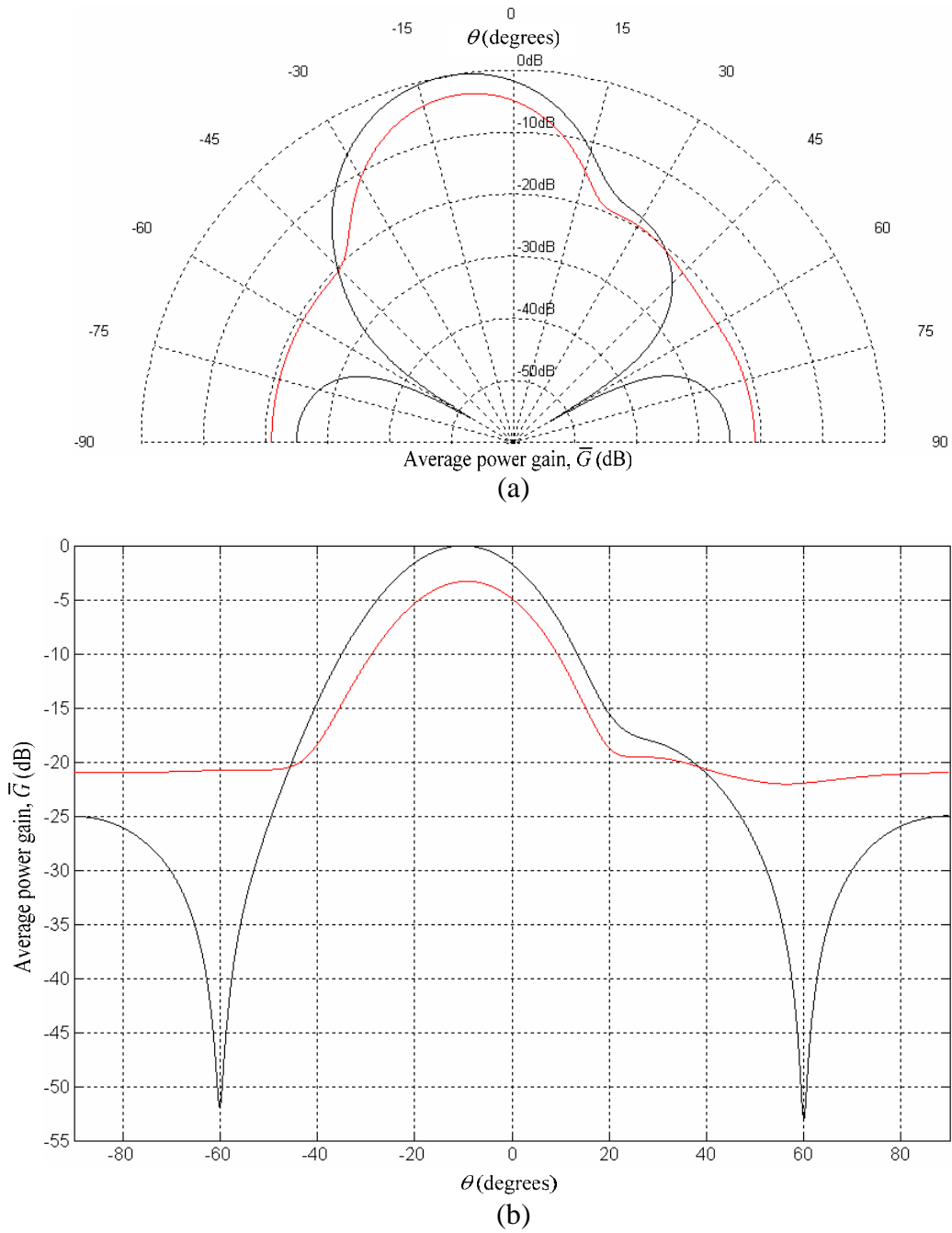and interference rejection level.

(a)

(b)

——— Absence of position errors and sensor node failures

——— Presence of position errors ($\Delta d = 0.3\lambda$) and 15 sensor node failures

2-D plots generated at $\phi = 45°$

Figure 37.   Average power gain of the beams generated by the 7×7 sensor cluster in the presence of position errors $\Delta d = 0.3\lambda$ and fifteen sensor node failures at $\left(\theta_0, \phi_0\right) =$ $\left(-10°, 45°\right)$: (a) Polar plots and (b) X-Y plots showing the decrease in maximum average power gain and interference rejection level.
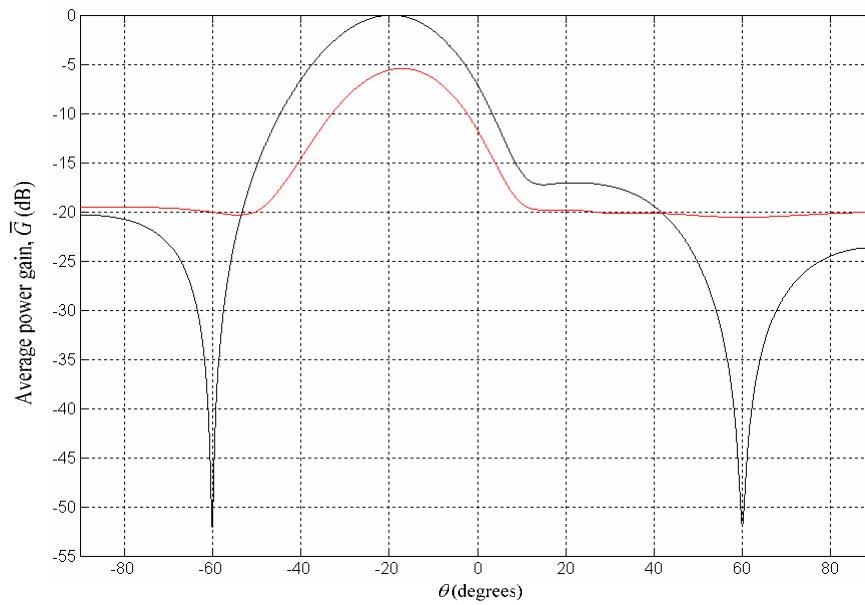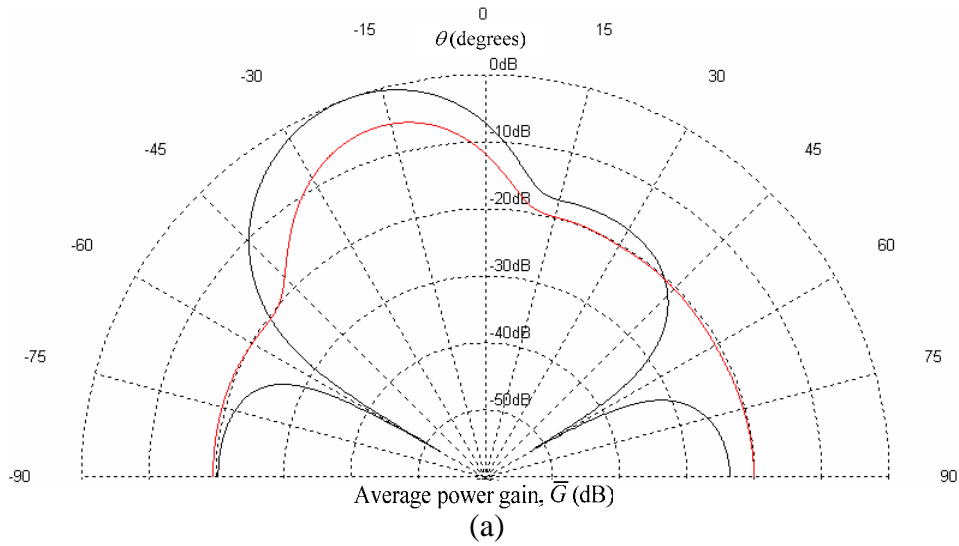
(a)

(b)

—— Absence of position errors and sensor node failures
—— Presence of position errors ($\Delta d = 0.4\lambda$) and 20 sensor node failures

2-D plots generated at $\phi = 45°$

Figure 38.   Average power gain of the beams generated by the 7×7 sensor cluster in the presence of position errors $\Delta d = 0.4\lambda$ and twenty sensor node failures at $\left(\theta_0, \phi_0\right) =$ $\left(-20°, 45°\right)$: (a) Polar plots and (b) X-Y plots showing the decrease in maximum average power gain and interference rejection level and the presence of main lobe pointing error.
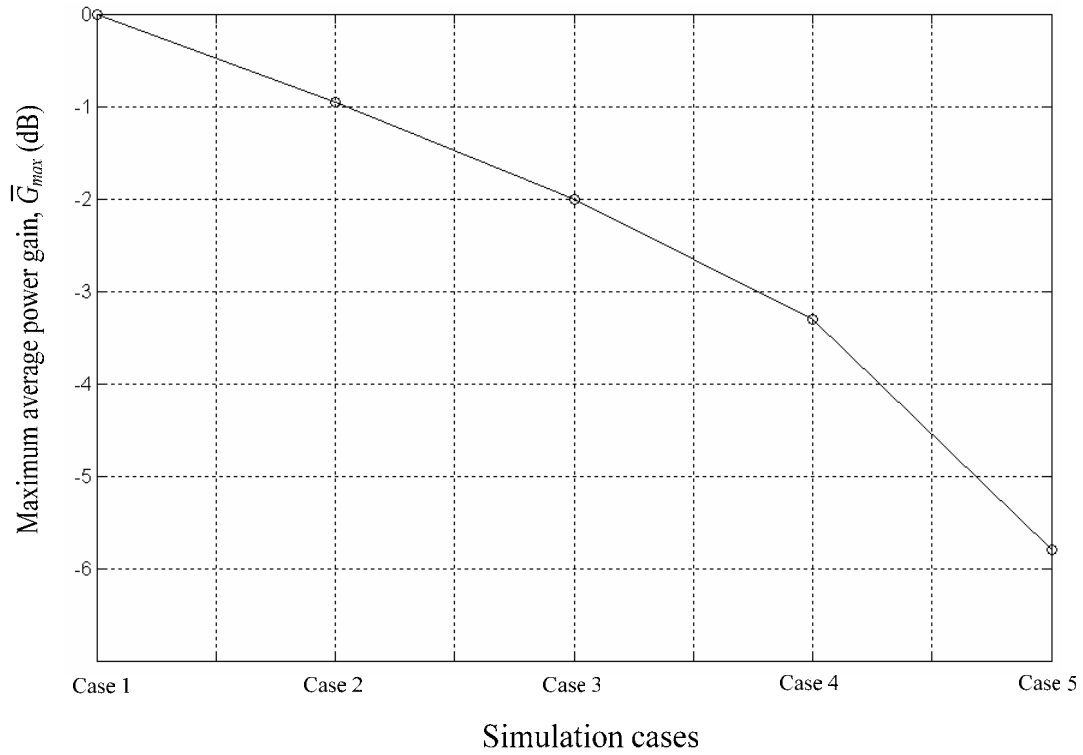
65

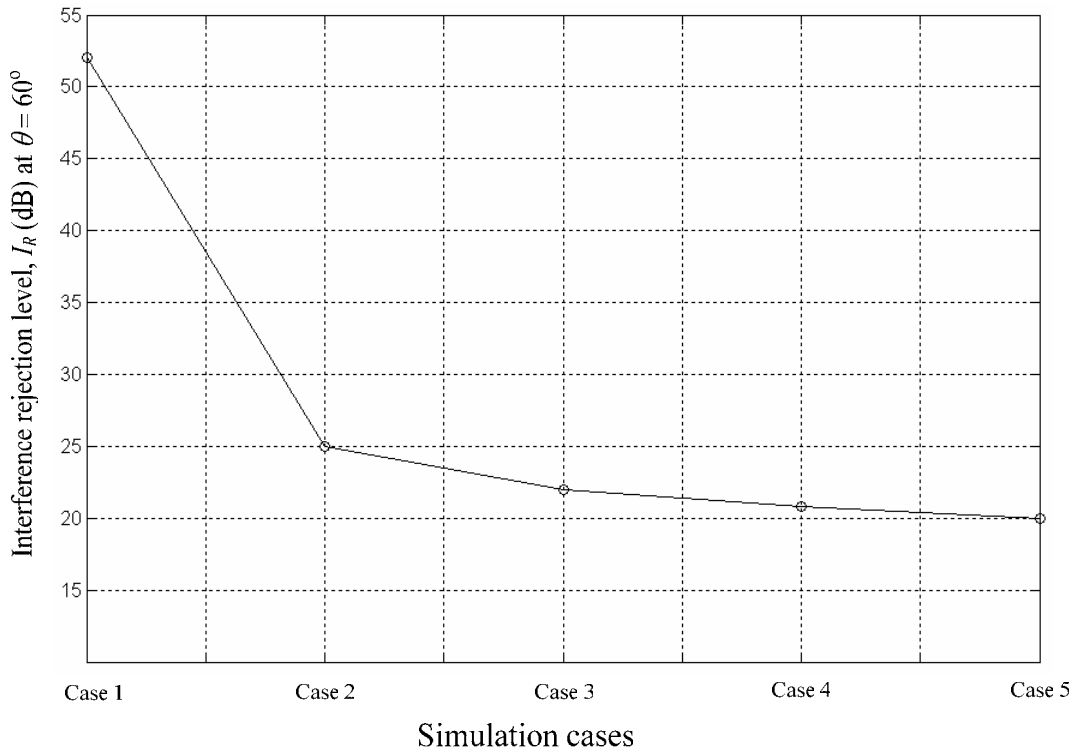Figure 39.   Reduction in maximum power gain with increase in Δd and sensor node failures.

Figure 40.   Reduction in interference rejection level with increase in Δd and sensor node failures.

66

G.   EFFECTS OF UAV SPEED ON THE ADAPTIVE ALGORITHM

The speed of the UAV has some influence over the performance of the algorithm used for adaptive beamforming. Figure 41 shows a plot of the magnitude of the squared error $\left|e^2(t)\right|$ versus the number of samples N_s. This plot shows the convergence trend of the algorithm as the number of samples increases. The mean square error is computed to be 0.0905 after 120 iterations which is below the convergence threshold, an indication of convergence. It was further assumed that the algorithm required 120 samples/s in order to reach convergence when the speed of the UAV was 40 m/s.

If the speed of the UAV were increased by a factor of two (becomes 80 m/s), the sampling rate would be reduced by the same factor (becomes 60 samples/s). Figure 42 shows the convergence of the LMS algorithm for this case. The mean square error is computed to be 0.1697 after 60 iterations which is above the convergence threshold. Figure 43 shows how the mean square error deteriorates when the speed of the UAV increases. This problem may be solved by increasing the sampling rate of the adaptive algorithm when the speed of the UAV increases. As shown in Fig. 43, the LMS can still converge at a sampling rate of 360 samples/s when the UAV speed is 120 m/s.
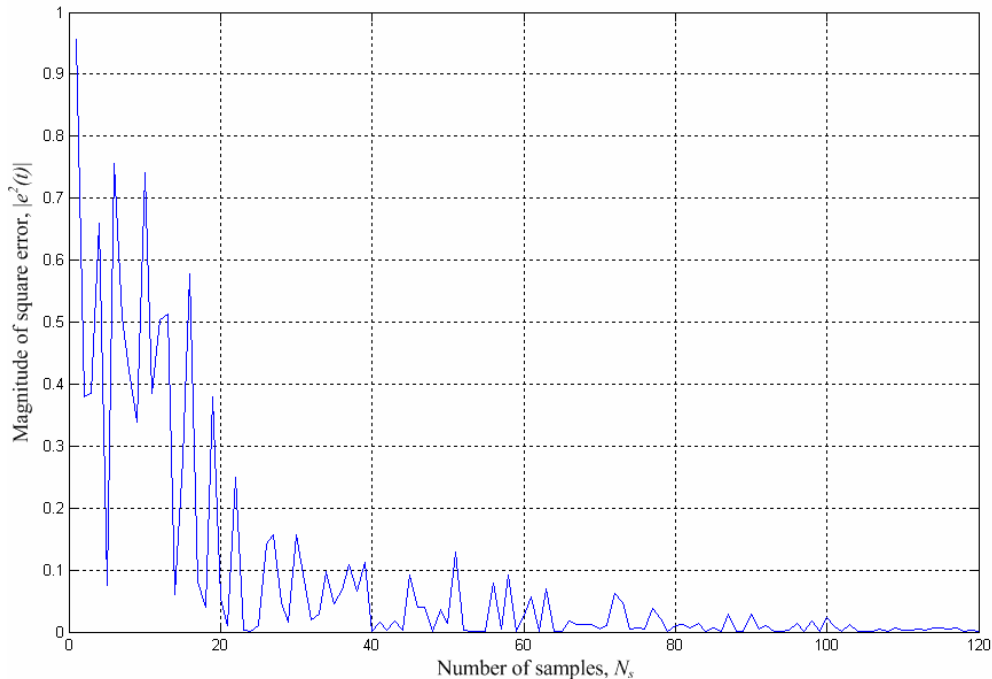

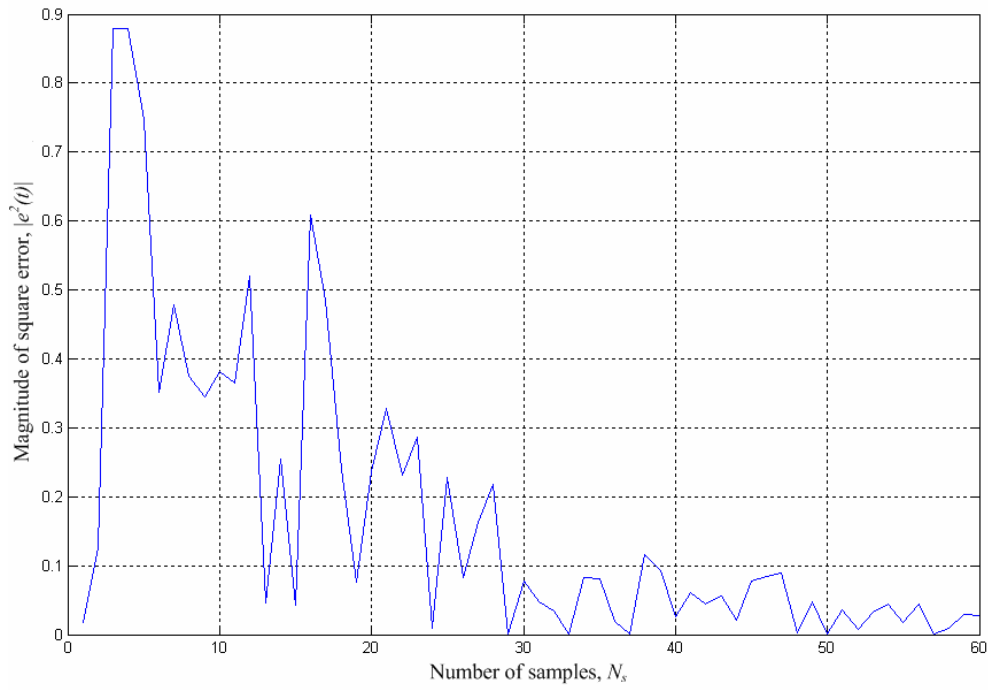Figure 41.   Convergence of the LMS algorithm at UAV speed of 40 m/s.

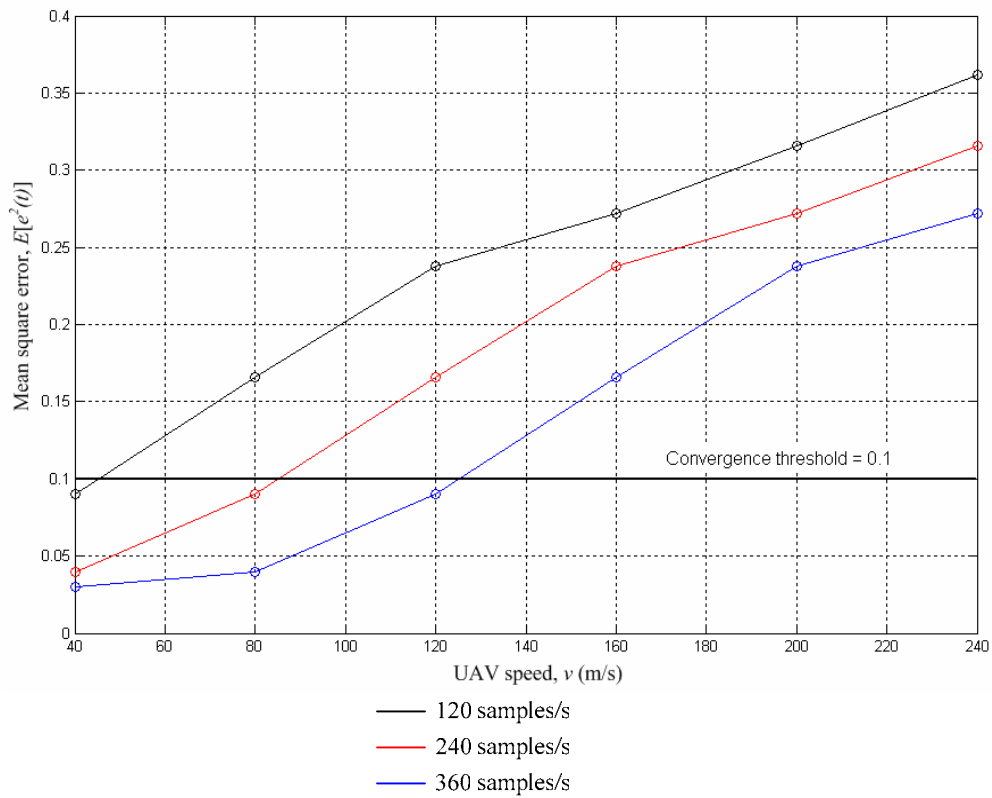Figure 42.   Convergence of the LMS algorithm at UAV speed of 80 m/s.

Figure 43.   Mean square error of the LMS algorithm at different UAV speed.

H. SUMMARY

This chapter presented the simulation model and the results. Simulation results showing the effects of the sensor node density, position errors and sensor node failures on the antenna beam generated by the sensor cluster were illustrated. Results showed that the average sidelobe levels increased while the maximum average power gain decreased when the density (i.e., number of sensor nodes per unit area) of the sensor nodes decreased. However, the shape of the main lobe remained relatively unchanged when the density changed. Results also showed that the presence of position errors and sensor node failures reduced the maximum average power gain of the antenna beam and increased its sidelobe levels, but the shape of the main lobe remained relatively unchanged. These simulation results were found to be in good agreement with the theoretical results for random arrays [7, 8].

A series of plots showing the adaptive beamforming capability of the sensor cluster were also illustrated. It was shown that the maximum average power gain and the interference rejection levels decreased when the position errors and the number of sensor node failures increased. Additionally, main lobe pointing error occurred when the position errors increased to 0.4λ and the number of sensor node failures increased to twenty.

Lastly, the significance of the sampling rate on the convergence of the LMS algorithm when the UAV speed increased was discussed.

THIS PAGE INTENTIONALLY LEFT BLANK

V. CONCLUSIONS

A wireless senor network (WSN) consists of a large number of small sensor nodes that are densely deployed over an area of interest to acquire information about targets of interest. These sensor nodes collaborate among themselves to form an ad-hoc network and disseminate the collected target information to an UAV. The objective is to increase the data rate and transmission range between the sensor nodes and the UAV. To meet this objective, a distributed beamforming approach was proposed whereby the sensor nodes are grouped into clusters and their transmission are coordinated in order to form a distributed antenna array that directs a beam towards the UAV.

A three-tiered hierarchical clustering sensor network architecture was considered in this thesis. A simulation model was developed and implemented in MATLAB programming language to study the application of beamforming using sensor clusters to establish a communication link with the UAV. Different sensor node densities, position errors and sensor node failures were simulated to investigate their effects on the antenna beam generated by the sensor cluster.

A.   SIGNIFICANT RESULTS

Results showed that the average sidelobe levels increased while the maximum average power gain decreased when the density (i.e., number of sensor nodes per unit area) of the sensor nodes decreased. However, the shape of the main lobe remained relatively unchanged when the density changed. Results also showed that the presence of position errors and sensor node failures reduced the maximum average power gain of the antenna beam and increased its sidelobe levels, but the shape of the main lobe remained relatively unchanged. These simulation results were found to be in good agreement with the theoretical findings for random arrays [7, 8].

Since the shape of the antenna main lobe remains relatively unchanged in the presence of position errors and sensor node failures or when the density of the sensor nodes changed, it can be steered towards the UAV in an adaptive manner as the UAV flew over the sensor field. This implied that the energy of the antenna beam can be di-

rected towards the UAV, resulting in higher signal-to-noise ratio, and, hence higher channel capacity. Additionally, the maximum average power gain of the main lobe can be increased by increasing the density of the sensor cluster, thereby increasing the transmission range between the sensor clusters and the UAV.

B. RECOMMENDATIONS FOR FUTURE WORK

It was assumed in this study that there was perfect frequency, phase, data synchronization and beamforming coordination among the sensor nodes within the cluster. This may be difficult to achieve in practice. The effects of these imperfections may be investigated in a future study.

The effects of mutual coupling on the antenna beam was also not considered in this study. In reality, some sensor nodes may be close to each other and the effects of mutual coupling on the antenna beam can be significant. These effects on the quality of the antenna beam may be investigated.

The beamforming process was implemented on the sensor clusters in this study. The same idea can be extended to the UAV so that the performance of the entire MIMO system can be evaluated.

APPENDIX   MATLAB PROGRAM FLOWCHART

This Appendix describes the flowchart of the MATLAB program used in this thesis work. Figure A.1 shows the main program flowchart and the sub-programs are described in the following discussions.
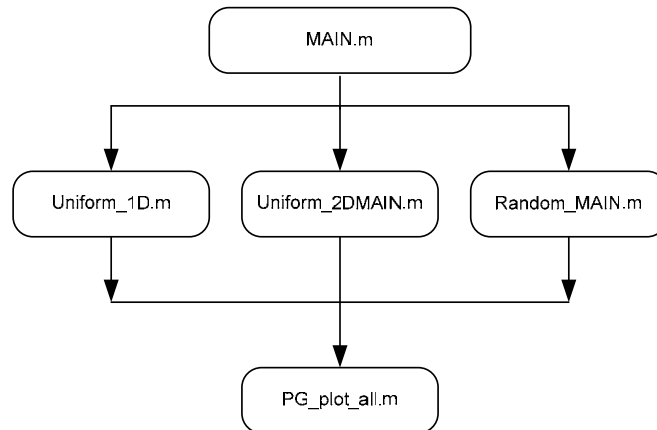
Figure A.1.   Main program flowchart

Uniform_1D.m

This program simulates the normalized power gain of a uniformly excited 10×1 omni-directional antenna array with equal element to element spacing.

Uniform_2DMAIN.m

This program simulates the normalized power gain of a uniformly excited $M \times N$ omni-directional antenna array with equal element to element spacing. The major limitation of this program is that the M must be equal to N.

Random_MAIN.m

This program simulates the average power gain of a random array with $M \times N$ elements subjected to random positioning, position errors and sensor node failures. The major limitation of this program is that the M must be equal to N.

PG_plot_all.m

This program produces all the antenna beam pattern plots contained in this thesis.

Figures A.2 and A.3 show the flowchart of the *Uniform_2DMAIN.m* program and the and the *Random_MAIN.m* program, respectively. The sub-programs are described as followed.

Uniform_2DLOC.m

This program generates the x and y-coordinates of the sensor nodes with equal element to element spacing.

Uniform_2DWts.m

This program generates the magnitude (all equal) and angle of the complex weights.

Uniform_2DAF_cal.m

This program computes the array factor of the sensor cluster.

PG_plot.m

This program produces the antenna beam pattern plot.

Random_LOC.m

This program generates the x and y-coordinates of the sensor nodes with random positions within the specified square area of length *L*.

LMS.m

This program computes the complex weights of the sensor cluster using LMS algorithm.

Random_FAIL.m

This program chooses *fail* number of elements from $N \times M$ elements and set the magnitude of their complex weights to zero.

AF_cal.m

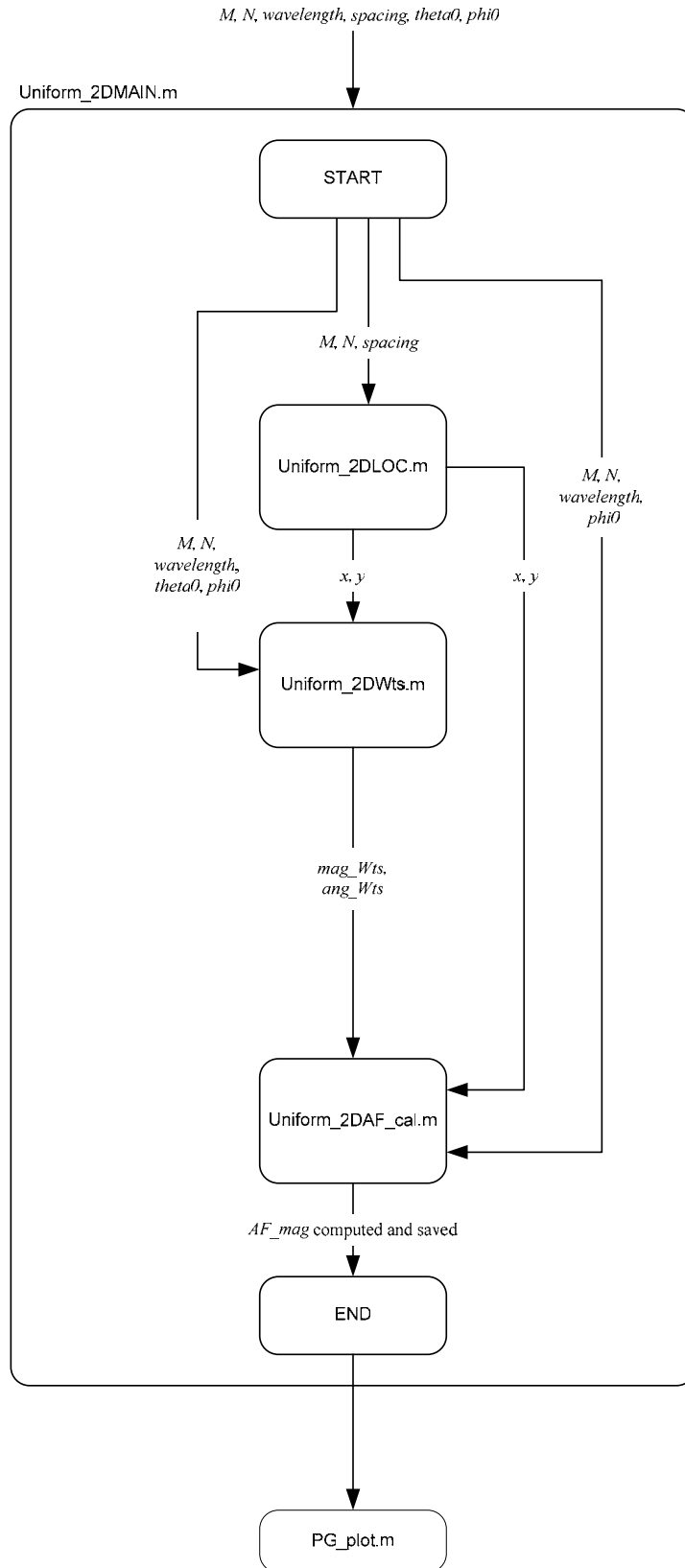This program computes the array factor of the sensor cluster.

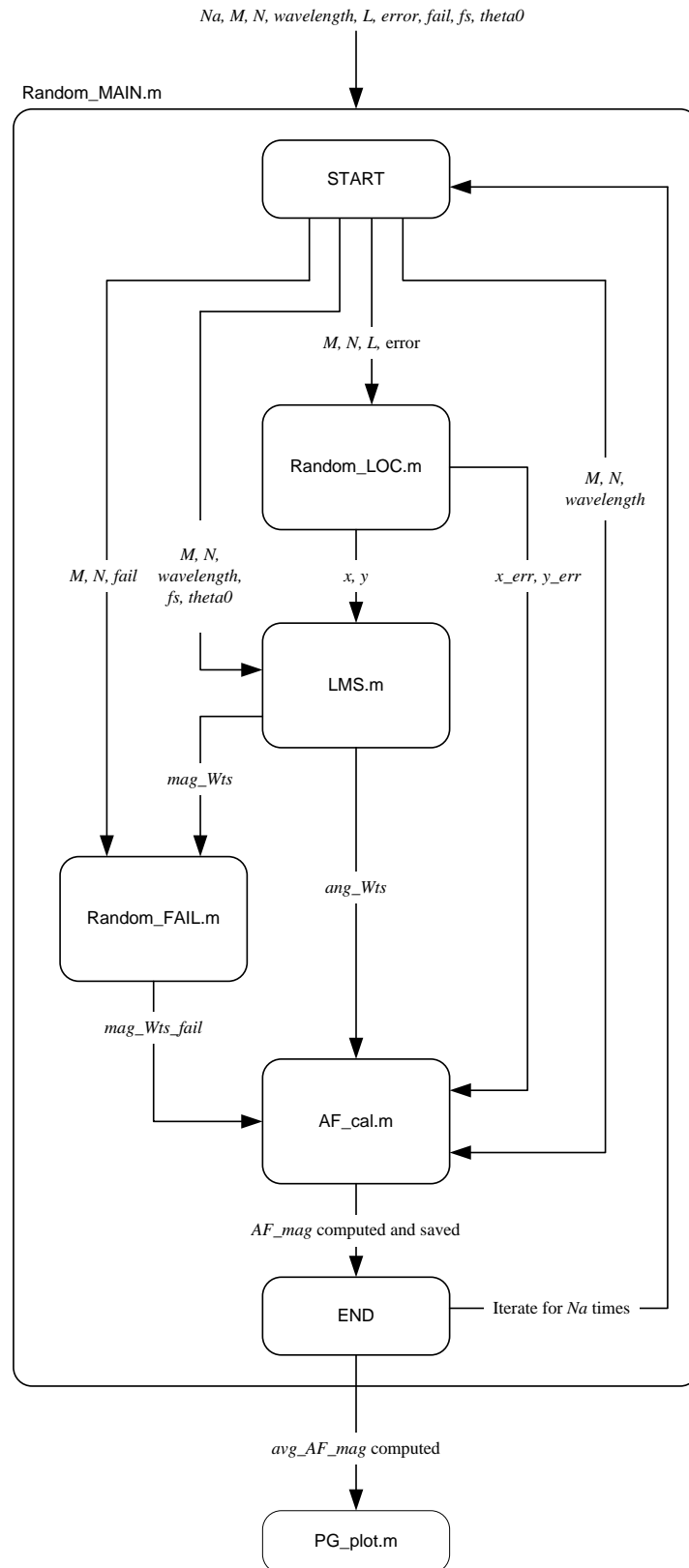Figure A.2.   Program flowchart for *Uniform_2DMAIN.m*

Figure A.3.   Program flowchart for *Random_MAIN.m*

76

PG_plot.m

This program produces the antenna beam pattern plot.

Description of variables

1. M = number of elements along x-axis

2. N = number of elements along y-axis

3. x = x-coordinates of the sensor node

4. x_err = x-coordinates of sensor node with errors (in meters)

5. y = y-coordinates of the sensor node

6. y_err = y-coordinates of sensor node with errors (in meters)

7. *wavelength* = design wavelength of the array (in meters)

8. L = length of square plane (in meters)

9. *error* = position errors (in meters)

10. *fail* = number of elements failure

11. *spacing* = element-element spacing along x-axis and y-axis

12. *theta0* = AOA elevation angle (in radians)

13. *phi0* = AOA azimuth angle (in radians)

14. Na = number of random array samples to be generated

15. fs = sampling rate

16. *mag_Wts* = magnitude of the complex weights

17. *mag_Wts_fail* = weights with magnitude of failed elements set to zero

18. *ang_Wts* = angle of the complex weights (in radians)

19. *AF_mag* = array factor

20. *avg_AF_mag* = average array factor

THIS PAGE INTENTIONALLY LEFT BLANK

LIST OF REFERENCES

[1]   I. F. Akyildiz, W. Su, Y. Sankarasubramaniam and E. Cayirci, "A Survey on sensor networks," *IEEE Communications Magazine*, Vol. 40, No. 8, pp. 102 – 114, 2002.

[2]   Chee-Yee Chong and Srikanta P. Kumar, "Sensor networks: evolution, opportunities and challenges," *Proceedings of the IEEE*, Vol. 91, No.8, pp. 1247 – 1256, 2003.

[3]   Bernard Sklar, *Digital Communications, Fundamentals and Applications*, Prentice Hall, New Jersey, 2001.

[4]   Beach, M.A., McNamara, D.P., Fletcher, P.N. and Karlsson, P., "MIMO-A solution for advanced wireless access," *11th International Conference on Antennas and Propagation*, Vol. 1, pp. 17 – 20, 2001.

[5]   J. S. Blogh and L. Hanzo, *Third-Generation Systems and Intelligent Wireless Networking, Smart Antennas and Adaptive Modulation*, IEEE Press, John Wiley & Sons, New York, 2002.

[6]   G. Barric, R. Mudumbai and U. Madhow, "Distributed beamforming for information transfer in sensor networks," *Proceedings of the Third International Symposium on Information Processing in Sensor Networks*, pp. 81 – 88, 2004.

[7]   Bernard D. Steinberg, *Principles of Aperture and Array System Design, including Random and Adaptive Arrays*, John Wiley & Sons, New York, 1976.

[8]   John Litva and Titus Kwok-Yeung Lo, *Digital Beamforming in Wireless Communications*, Artech House, Norwood, MA, 1996.

[9]   Chien-Chung Shen, Chaiporn Jaikaeo and Chavalit Srisathapornphat, "Sensor information networking architecture and applications," *IEEE Personal Communications*, Vol. 8, No. 4, pp. 52 – 59, 2001.

[10]   Jianping Pan, Y. Thomas Hou, Lin Cai, Yi Shi and Sherman X. Shen, "Topology control for wireless sensor networks," *Proceedings of the 9th Annual International Conference on Mobile Computing and Networking*, San Diego, CA, USA, pp. 286 – 299, 2003.

[11]   M. Tubaishat and S. Madria, "Sensor networks: An overview," *IEEE Potentials*, Vol. 22, No. 2, pp. 20 – 23, 2003.

[12]   Quanhong Wang, Hossam Hassanein and Kenan Xu, "A Practical Perspective on Wireless Sensor Networks," in *Handbook of Sensor Networks: Compact Wireless and Wired Sensing Systems*, edited by Mohammad Ilyas and Imad Mahgoub, chapt. 9, CRC Press, Florida, 2005.

[13]   Mark Yarvis and Wei Ye, "Tiered Architecture in Sensor Networks," in *Handbook of Sensor Networks: Compact Wireless and Wired Sensing Systems*, edited by Mohammad Ilyas and Imad Mahgoub, chapt. 13, CRC Press, Florida, 2005.

[14]   Ekram Hossain, Rajesh Palit and Parimala Thulasiraman, "Clustering in Mobile Wireless Ad Hoc Networks," in *Wireless Communications Systems and Networks*, edited by Mohsen Guizani, pp. 383 – 424, Kluwer Academic Pub., New York, 2004.

[15]   C. Siva Ram Murthy and B. S. Manoj, *Ad Hoc Wireless Networks, Architectures and Protocols*, Prentice Hall, New Jersey, 2004.

[16]   Farinaz Koushanfar, Sasa Slijepcevic, Miodrag Potkonjak and Alberto Sangiovanni-Vincentelli, "Location Discovery in Ad-hoc Wireless Sensor Networks," in *Ad Hoc Wireless Networking*, Xiuzhen Cheng, Xiao Huang and Ding-Zhu Du, pp. 137 – 173, Kluwer Academic Pub., New York, 2004.

[17]   Lal C. Godara, "Application of antenna arrays to mobile communications, Part II: Beam-forming and direction-of-arrival considerations," *Proceedings of the IEEE*, Vol. 85, No. 8, pp. 1195 – 1245, 1997.

[18]   Warren L. Stutzman and Gary A. Thiele, *Antenna Theory and Design*, John Wiley & Sons, New York, 1998.

[19]   Harry L. Van Trees, *Optimum Array Processing, Part IV of Detection, Estimation, and Modulation Theory*, John Wiley & Sons, New York, 2002.

[20]   Ramakrishna Janaswamy, *Radiowave Propagation and Smart Antennas for Wireless Communications*, Kluwer Academic Publishers, Boston, 2001.

[21]   Z. Yifeng, P. C. Yip and H. Leung, "Tracking the direction-of-arrival of multiple moving targets by passive arrays: Algorithm," *IEEE Trans. Signal Processing*, Vol. 47, pp. 2655 – 2666, 1999.

[22]   C. K. Sword, M. Simaan and E. W. Kamen, "Multiple target angle tracking using sensor array output," *IEEE Trans. Aerosp. Electron. Syst*., Vol. 26, pp. 367 – 372, 1990.

[23]   C. R. Rao, L. Zhang and L. C. Zhao, "Multiple target angle tracking using sensor arrays output," *IEEE Trans. Aerosp. Electron. Syst*., Vol. 29, pp. 268 – 271, 1993.

[24]   S. B. Park, C. S. Ryu and K. K. Lee, "Multiple target tracking algorithm using predicted angles," *IEEE Trans. Aerosp. Electron. Syst*., Vol. 30, pp. 643 – 648, 1994.

THIS PAGE INTENTIONALLY LEFT BLANK

INITIAL DISTRIBUTION LIST

1. Defense Technical Information Center
   Ft. Belvoir, Virginia

2. Dudley Knox Library
   Naval Postgraduate School
   Monterey, California

3. Professor John P. Powers, Chairman, Code EC
   Department of Electrical and Computer Engineering
   Naval Postgraduate School
   Monterey, California

4. Professor Murali Tummala, Code EC/Tu
   Department of Electrical and Computer Engineering
   Naval Postgraduate School
   Monterey, California

5. Professor Roberto Cristi, Code EC/Cx
   Department of Electrical and Computer Engineering
   Naval Postgraduate School
   Monterey, California

6. Professor Yeo Tat Soon
   Director
   Temasek Defence Systems Institute
   Block E1, #05-05
   Singapore

7. Chan Chee Wai
   Singapore